Journal of *Marine Science and Engineering*

MDPI

Article

A Subnetwork-Node-Constrained Hydrophone Positioning Method for Towed-Streamer Seismic Exploration

Haonan Zhang [1,2,3], Lingsheng Lv [1], Cuilin Kuang [1,*], Baocai Yang [1,2], Heng Liu [1] and Guo Guo [1]

[1] School of Geosciences and Info-Physics, Central South University, Changsha 410083, China; zhanghn7@cosl.com.cn (H.Z.); lingshenglv2024@163.com (L.L.); ex_yangbc@cnooc.com.cn (B.Y.); mesliuheng@163.com (H.L.); doubleguo@csu.edu.cn (G.G.)
[2] Geophysical Division of China Oilfield Services Ltd., Tianjin 300451, China
[3] National Engineering Research Center of Offshore Oil and Gas Exploration, Beijing 100028, China
* Correspondence: kuangcuilin@csu.edu.cn

Abstract

Accurate hydrophone positioning is essential for the quality of marine seismic imaging and the reliability of structural interpretation. To mitigate the accuracy degradation of the conventional polynomial model under unevenly distributed or missing acoustic observations, we propose a hydrophone positioning method that incorporates subnetwork node constraints. An iterated extended Kalman filter (IEKF) estimates the acoustic node coordinates and their full within-subnetwork posterior covariances, which serve as weighted virtual observations in a global polynomial adjustment. In a straight-line simulation, the mean front/rear node deviations decrease from 1.83/1.25 m with the polynomial model to 0.28/0.47 m, and the mean hydrophone deviation decreases by 19.0%/24.7% relative to the polynomial and hybrid harmonic function models. Field datasets A/B show lower node discrepancies and mean hydrophone discrepancy reductions of 18.8%/22.9% versus the polynomial model and 16.5%/18.1% versus the hybrid harmonic function model, relative to commercial references. These percentages are specific to the sequences examined. Paired statistics that account for temporal dependence support positive mean reductions across all tested block lengths. The method maintains low deviations under the tested persistent observation loss, with computation times comparable to those of the polynomial model. These results indicate lower simulated deviations and closer agreement with commercial references under the evaluated conditions.

Keywords: hydrophone positioning; polynomial positioning model; subnetwork node constraints; towed-streamer seismic exploration

Check for updates

Academic Editors: Chung-Ru Ho and Manuel Martín-Martín

Received: 19 August 2026
Revised: 3 October 2026
Accepted: 20 October 2026
Published: 23 October 2026

Copyright: © 2026 by the authors. Licensee MDPI, Basel, Switzerland. This article is an open access article distributed under the terms and conditions of the Creative Commons Attribution (CC BY) license.

1. Introduction

Global deep-sea oil and gas exploration remains active, and deep-sea resources have become an important source of newly discovered hydrocarbon reserves [1]. As China advances its maritime development strategy, strengthening its capacity for independent deep-sea oil and gas exploration and development is vital for national energy security [2,3]. Marine towed-streamer seismic exploration is a key means of obtaining high-resolution images of subsurface geological structures [4,5], and domestic control over its core equipment is therefore particularly critical. The Haijing integrated towed-streamer seismic exploration system, independently developed by the China National Offshore Oil Corporation (CNOOC), has been deployed on several seismic vessels and entered commercial service, marking substantial progress in this field [6]. During a typical survey, a seismic vessel

tows a source array and multiple long streamers along predetermined survey lines, while hydrophones mounted on the streamers record seismic waves reflected from subsurface strata [7]. Hydrophone positioning deviations affect reflection point positioning and bin assignment. Accurate determination of hydrophone positions at each shot epoch is therefore fundamental to reliable marine seismic data processing and imaging [8].

Early studies of towed-streamer hydrophone positioning mainly adopted a two-step, or numerical, approach. Acoustic node coordinates were first determined by network adjustment, after which hydrophone positions between nodes were calculated through coordinate integration or interpolation. Yao et al. [9] proposed a progressive strategy comprising constrained network adjustment, curve integration, and quasi-stable adjustment. Yi et al. [10,11] and Xu [12] systematically investigated gross-error detection, filtering, smoothing, and acoustic network adjustment for navigation data. Zhang et al. [13] and Zhang et al. [7] examined integrated navigation networks for multi-source, multi-streamer surveys and their preprocessing procedures. Sang et al. [14] compared the performance of different numerical positioning models. The two-step approach has a clear workflow and is convenient to implement in separate stages. However, node estimation and hydrophone interpolation are usually performed separately, so the propagation of node uncertainty and correlations into the subsequent streamer-shape calculation must be explicitly addressed in the model.

Analytical approaches instead represent streamer shape using continuous functions and estimate their parameters from positioning observations. Gilbert [15] used polynomial functions to describe the horizontal shape of a single streamer, while Egeland [16] represented the streamer as a three-dimensional curve and obtained coordinates by integrating fitted azimuth and depth information. For multi-streamer positioning, Zinn and Rapatz [17] combined compass and acoustic observations in a global network solution using a segmented circular-arc representation and an extended Kalman filter. Gikas [18] and Gikas et al. [19] further developed polynomial and Kalman-filtering approaches for source and streamer positioning. More recent studies have explored alternative curve representations and adjustment formulations. Yu et al. [20] established a polynomial curve-fitting positioning model and Duan et al. [21] developed a curve-integration-based method. Zhang et al. [22] introduced a spline curve-fitting model, while Sang et al. [23] proposed a hybrid harmonic function model. These developments provide different ways to represent streamer geometry and incorporate multiple observation types into positioning.

Despite these developments, unevenly distributed or locally missing acoustic observations can leave some streamer sections weakly constrained, and their effects may propagate to other positions through the estimated curve parameters. Making effective use of the acoustic networks and position references at the streamer ends, while retaining a continuous representation of the entire streamer, therefore offers a means of improving hydrophone positioning. This study targets post-mission positioning during straight-line towed-streamer operations and introduces subnetwork node constraints into the polynomial analytical positioning model. Local acoustic subnetworks are constructed near the gun arrays and at the streamer tails, and an iterated extended Kalman filter (IEKF) estimates their node coordinates and posterior covariance matrices, which are then introduced as weighted virtual observations into the global polynomial adjustment. By transferring local filtering information through node coordinates and covariance matrices, the method connects node estimation at the streamer ends with the estimation of global curve parameters. The polynomial representation is retained, and the study focuses on the effects of subnetwork constraints on node and hydrophone positioning.

Section 2 describes subnetwork node estimation, the globally constrained adjustment, and the positioning deviation metrics. Section 3 compares the methods using simulated data and field data from two survey areas and examines the effects of covariance inflation,

acoustic observation loss, and computation time. Section 4 discusses the experimental results and the applicability of the method. Section 5 presents the conclusions.

2. Methodology

The towed-streamer positioning network consists of several types of positioning equipment working together, as illustrated in Figure 1. The Differential Global Navigation Satellite System (DGNSS) and gyrocompasses determine the position and attitude of the survey vessel. The Relative Global Navigation Satellite System (RGNSS) transfers the vessel-based position reference to the gun arrays and tail buoys. Compass birds measure the tangential magnetic azimuth at their locations, while acoustic transducers obtain acoustic distances through two-way ranging. Compass birds also carry depth sensors that measure their depth below the sea surface. In addition to these positioning sensors, hydrophones are mounted at regular intervals along each streamer to acquire reflected seismic data. Determining their spatial positions requires combining the position references provided by DGNSS and RGNSS with compass azimuths and acoustic distances to reconstruct the streamer shape. Hydrophone array positioning is therefore essentially a process of reconstructing streamer geometry.

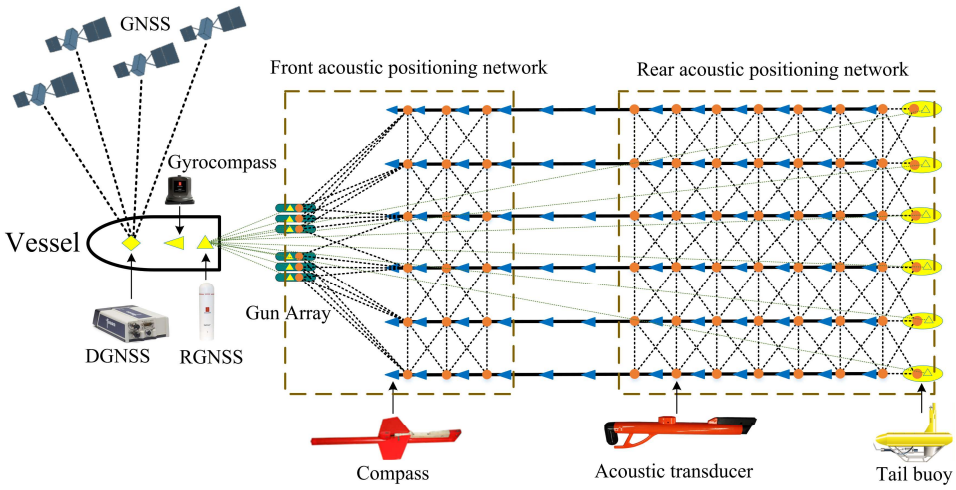

Figure 1. Schematic diagram of the towed-streamer positioning network for marine seismic exploration.

2.1. Positioning of Front and Rear Subnetwork Acoustic Nodes Based on IEKF

Figure 2 illustrates the front and rear subnetwork positioning configurations. The front subnetwork consists of the acoustic nodes on the gun arrays and at the streamer heads. The gun-array nodes serve as position references, and the solution uses acoustic distances and line-of-sight azimuths derived from preprocessed coordinates. The rear subnetwork consists of the acoustic nodes on the tail buoys and selected acoustic nodes near the streamer tails. The tail-buoy nodes serve as the position references, and the solution likewise uses acoustic distances and line-of-sight azimuths derived from preprocessed coordinates. Subnetwork nodes are selected according to the actual configuration of each dataset, as detailed in Section 3. Before positioning, the RGNSS data, acoustic distances, compass observations, and relevant node coordinates are preprocessed. Magnetic declination corrections and angular wraparound handling are also applied to the compass observations [24].

Figure 3 shows the local coordinate system used for positioning. Its origin is the vessel position center, denoted by NRP, and its axes are parallel to the projected northing and easting directions. All subsequent calculations are performed in this local coordinate system. The coordinates are converted to the Earth-centered, Earth-fixed coordinate system

only when the final hydrophone positions are output. Before the positioning solution at each epoch, the head and tail reference positions, streamer configuration, and compass observations are used to propagate coordinates from the head toward the tail and from the tail toward the head. The two estimates are then combined by weighting to obtain preprocessed coordinates and their uncertainties at any point along each streamer [24].

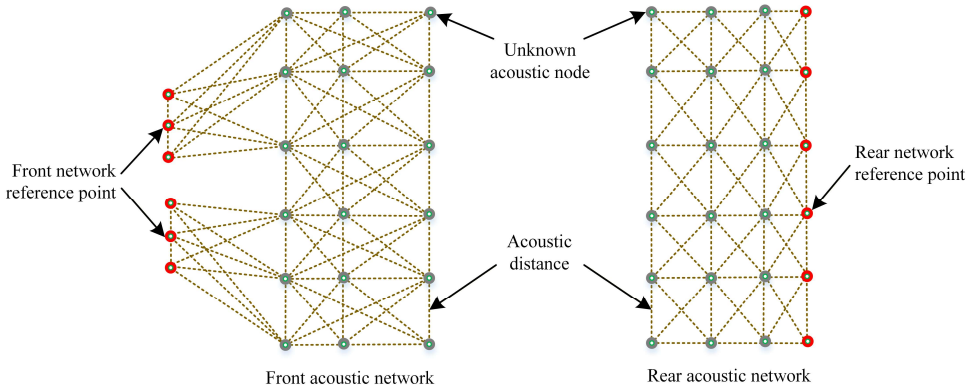

Figure 2. Schematic diagram of the front and rear subnetworks.

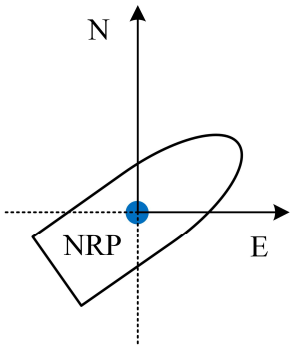

Figure 3. Local coordinate system used for the network solution.

The RGNSS equipment on the gun arrays and tail buoys provides position references for the front and rear subnetworks. In the local acoustic networks, the gun-array and tail-buoy acoustic nodes serve as known control points for the front and rear subnetworks, respectively. The streamers are equipped with depth-control devices, and the depths of individual sensors are obtained by interpolating depth sensor observations along the streamer [24]. The state vector therefore consists of the planar coordinates of the unknown acoustic nodes. For a front or rear subnetwork containing m unknown acoustic nodes, the state vector at epoch k is defined as

$$\boldsymbol{X}_k = [N_1, E_1, \ldots, N_m, E_m]^T \tag{1}$$

Under straight-line operating conditions with short epoch intervals, the streamer shape relative to the vessel position center at the preceding epoch can serve as the prior mean for the current epoch. A random-walk state model is adopted:

$$\begin{aligned} \boldsymbol{X}_k &= \boldsymbol{F}_{k,k-1}\boldsymbol{X}_{k-1} + \boldsymbol{w}_k \qquad (\boldsymbol{w}_k \sim N(0, \boldsymbol{Q})) \\ \hat{\boldsymbol{X}}_k^- &= \boldsymbol{F}_{k,k-1}\hat{\boldsymbol{X}}_{k-1}^+ \qquad \boldsymbol{P}_k^- = \boldsymbol{F}_{k,k-1}\boldsymbol{P}_{k-1}^+\boldsymbol{F}_{k,k-1}^T + \boldsymbol{Q} \end{aligned} \tag{2}$$

The solution is performed in a coordinate system centered on the vessel, with axes parallel to the northing and easting directions. Overall vessel translation therefore does not directly appear as node displacement in this coordinate system. During straight-line operations, when changes in streamer shape between adjacent epochs are small, the state

transition matrix $\boldsymbol{F}_{k,k-1}$ is approximated by the identity matrix. Node positions relative to the vessel at the preceding epoch are used as the predictions for the current epoch, while unmodeled relative motion is represented by the process noise $\boldsymbol{w}_k$. Here, $\hat{\boldsymbol{X}}_{k-1}^{+}$ and $\boldsymbol{P}_{k-1}^{+}$ are the state estimate and its variance–covariance matrix at the preceding epoch, and $\hat{\boldsymbol{X}}_{k}^{-}$ and $\boldsymbol{P}_{k}^{-}$ are their predicted counterparts at the current epoch.

The streamer head is more tightly controlled and generally has lower motion uncertainty. The tail is farther from the towing point and can undergo greater lateral motion under ocean currents, resulting in higher motion uncertainty. Accordingly, the process noise matrix $\boldsymbol{Q}$ for a survey line is determined from changes in the two-dimensional node coordinate components between adjacent epochs recorded in the P2/94 data [25]. This setting approximates the variability of node motion relative to the vessel. For each node, consecutive increments of the northing and easting coordinates are calculated in the local coordinate system. For a sequence of K epochs, the coordinate increments of node i at epoch k and their means are

$$\begin{aligned} \Delta N_{i,k} &= N_{i,k} - N_{i,k-1}, & \Delta E_{i,k} &= E_{i,k} - E_{i,k-1}, \\ \mu_{\Delta N,i} &= \frac{1}{K-1}\sum_{k=2}^{K} \Delta N_{i,k}, & \mu_{\Delta E,i} &= \frac{1}{K-1}\sum_{k=2}^{K} \Delta E_{i,k} \end{aligned} \tag{3}$$

After removing the mean increments, unbiased sample variances are calculated separately for the northing and easting components. The node-specific matrices are then assembled into a block-diagonal process noise matrix:

$$\begin{aligned} s_{\Delta N,i}^2 &= \frac{1}{K-2}\sum_{k=2}^{K}\left(\Delta N_{i,k} - \mu_{\Delta N,i}\right)^2 \qquad s_{\Delta E,i}^2 = \frac{1}{K-2}\sum_{k=2}^{K}\left(\Delta E_{i,k} - \mu_{\Delta E,i}\right)^2 \\ \boldsymbol{Q}_i &= diag\left(s_{\Delta N,i}^2, s_{\Delta E,i}^2\right) \qquad \boldsymbol{Q} = blkdiag\left(\boldsymbol{Q}_1, \ldots, \boldsymbol{Q}_m\right) \end{aligned} \tag{4}$$

This construction assigns node-specific process noise to the front and rear nodes based on their observed coordinate variations. Process noise is estimated offline from the complete sequence, once per dataset, and held fixed throughout the corresponding method comparisons and parameter tests. Appendix A lists the process noise standard deviations of the northing and easting coordinates for each estimated node in the experiments. The diagonal entries of $\boldsymbol{Q}$ are the squares of these standard deviations, expressed in m^2. The coordinate increments may contain both actual vessel-relative node motion and epoch-to-epoch changes in the commercial coordinate errors. Accordingly, $\boldsymbol{Q}$ is an empirical covariance of the observed increments rather than a separately identified covariance of physical motion. In the field experiments, the same P2/94 sequence is also used as the node reference, so process noise calibration and node evaluation are not independent.

State estimation requires a nonlinear relationship between the observations and the state vector, which is linearized to obtain the error equations. The nonlinear observation model is

$$\boldsymbol{Z}_k = h(\boldsymbol{X}_k) + \varepsilon_k, \qquad \varepsilon_k \sim N(0, \boldsymbol{R}_k) \tag{5}$$

Here, $\boldsymbol{Z}_k$ is the observation vector, h is the measurement function, $\boldsymbol{X}_k$ is the state vector, and ε_k is the measurement noise. The measurement noise covariance matrix $\boldsymbol{R}_k$ is determined from the nominal precision of the sensors. After the state prediction and its covariance at epoch k have been obtained through the time update in Equation (2), the current observations are used to iteratively refine the state estimate as follows:

(1) Linearization of the measurement model: The measurement function and its Jacobian are evaluated at the current estimate $\hat{\boldsymbol{X}}_k^{(q)}$:

$$\begin{aligned} \boldsymbol{l}_k^{(q)} &= \boldsymbol{Z}_k - h(\hat{\boldsymbol{X}}_k^{(q)}) \\ \boldsymbol{H}_k^{(q)} &= \left.\frac{\partial h}{\partial \boldsymbol{X}}\right|_{\boldsymbol{X}=\hat{\boldsymbol{X}}_k^{(q)}} \end{aligned} \tag{6}$$

where $\boldsymbol{l}_k^{(q)}$ is the measurement innovation vector for the current iteration.

(2) Kalman gain matrix:

$$\boldsymbol{K}_k^{(q)} = \boldsymbol{P}_k^- (\boldsymbol{H}_k^{(q)})^T \left[\boldsymbol{H}_k^{(q)} \boldsymbol{P}_k^- (\boldsymbol{H}_k^{(q)})^T + \boldsymbol{R}_k \right]^{-1} \tag{7}$$

where $\boldsymbol{R}_k$ is the measurement noise covariance matrix.

(3) State update: The predicted state is corrected using the measurement innovation and the re-linearization term

$$\begin{aligned} \hat{\boldsymbol{X}}_k^{(q+1)} &= \hat{\boldsymbol{X}}_k^- + \boldsymbol{K}_k^{(q)} \left[\boldsymbol{l}_k^{(q)} + \boldsymbol{H}_k^{(q)} (\hat{\boldsymbol{X}}_k^{(q)} - \hat{\boldsymbol{X}}_k^-) \right] \\ \boldsymbol{P}_k^{(q+1)} &= (\boldsymbol{I} - \boldsymbol{K}_k^{(q)} \boldsymbol{H}_k^{(q)}) \boldsymbol{P}_k^- \end{aligned} \tag{8}$$

Within each epoch, the predicted covariance $\boldsymbol{P}_k^-$ remains fixed during the iterations. Only the linearization point, Jacobian, and Kalman gain are updated. The final state estimate and its corresponding covariance are taken as the a posteriori results for that epoch.

At the first epoch, the initial covariance is set to the identity matrix, and the initial estimate at $q = 0$ is obtained from the preprocessed approximate coordinates, which are calculated by coordinate integration using compass-bird azimuths. From the second epoch onward, the a posteriori state from the preceding epoch forms the basis of the current prediction. The maximum number of IEKF iterations is set to 10. The subnetwork solution is considered converged when the difference between two consecutive state estimates satisfies $\left\| \hat{\boldsymbol{X}}_k^{q+1} - \hat{\boldsymbol{X}}_k^q \right\|_2 < 0.01$ m. If this threshold is not met within the maximum number of iterations, iteration stops and the subnetwork result is not used as a virtual node constraint at the current epoch.

The subnetwork adjustment mainly uses in-line and cross-line acoustic distances and line-of-sight azimuths derived from compass observations. First-order Taylor expansion of the observation equations at the approximate node coordinates yields the following three types of linearized error equations.

(1) Gun–streamer (or tail–streamer) acoustic distance observation equation: let the acoustic distance observation between a known reference point $G_m(N_{G_m}, E_{G_m}, U_{G_m})$ and the unknown node $P_i(N_i, E_i, U_i)$ be $r_{P_iG_m}^{obs}$. The corresponding error equation is

$$v_{r,P_iG_m} = \rho_{P_iG_m} - r_{P_iG_m}^{obs} = \frac{N_i^0 - N_{G_m}}{\rho_{P_iG_m}^0} dN_i + \frac{E_i^0 - E_{G_m}}{\rho_{P_iG_m}^0} dE_i - l_{r,P_iG_m} \tag{9}$$

Here, v_{r,P_iG_m} is the correction to the acoustic distance observation, and $\rho_{P_iG_m}$ is the computed acoustic distance. The quantities (N_i^0, E_i^0) are the approximate planar coordinates of the unknown node P_i, and $[dN_i, dE_i]$ are their corrections. The misclosure is $l_{r,P_iG_m} = R_{P_iG_m}^{obs} - \rho_{P_iG_m}^0$, where $\rho_{P_iG_m}^0 = \sqrt{(N_i^0 - N_{G_m})^2 + (E_i^0 - E_{G_m})^2 + (U_i - U_{G_m})^2}$ is the distance calculated from the approximate coordinates.

(2) Streamer–streamer acoustic distance observation equation: let the acoustic distance observation between two unknown nodes $P_i(N_i, E_i, U_i)$ and $P_j(N_j, E_j, U_j)$ be R_{ij}^{obs}; the error equation is

$$v_{r,ij} = \rho_{ij} - r_{ij}^{obs} = \frac{N_i^0 - N_j^0}{\rho_{ij}^0} (dN_i - dN_j) + \frac{E_i^0 - E_j^0}{\rho_{ij}^0} (dE_i - dE_j) - l_{r,ij} \tag{10}$$

Here, $v_{r,ij}$ is the correction to the acoustic distance observation and $\rho_{P_iP_j}$ is the computed distance. The quantities (N_i^0, E_i^0) and (N_j^0, E_j^0) are the approximate coordinates of nodes P_i and P_j, respectively, and $[dN_i, dE_i]$ and $\left[dN_j, dE_j\right]$ are the corresponding coordinate corrections. The misclosure is $l_{r,ij} = r_{ij}^{obs} - \rho_{P_IP_J}^0$, with $\rho_{ij}^0 = \sqrt{(N_i^0 - N_j^0)^2 + \left(E_i^0 - E_j^0\right)^2 + \left(U_i - U_j\right)^2}$.

(3) Azimuth observation equation: For adjacent acoustic nodes $P_i(N_i, E_i)$ and $P_j(N_j, E_j)$ on the same streamer, the observed line-of-sight azimuth and its uncertainty are derived from the preprocessed coordinates obtained using compass observations [14]. The corresponding error equation is

$$\begin{aligned} v_{\alpha,ij} &= \theta_{ij} - \alpha_{ij}^{obs} = -\frac{N_j^0 - N_i^0}{(D_{ij}^0)^2} dE_i + \frac{E_j^0 - E_i^0}{(D_{ij}^0)^2} dN_i + \frac{N_j^0 - N_i^0}{(D_{ij}^0)^2} dE_j - \frac{E_j^0 - E_i^0}{(D_{ij}^0)^2} dN_j - l_{\alpha,ij} \\ \alpha_{ij}^{obs} &= atan2(E_j^{PRe} - E_i^{PRe}, N_j^{PRe} - N_i^{PRe}) \end{aligned} \tag{11}$$

$$\delta_{\alpha_{ij}^{obs}} = \sqrt{\frac{\left(N_j^{pre} - N_i^{pre}\right)^2 \left(\delta_{E_i^{pre}}^2 + \delta_{E_j^{pre}}^2\right) + \left(E_j^{pre} - E_i^{pre}\right)^2 \left(\delta_{N_i^{pre}}^2 + \delta_{N_j^{pre}}^2\right)}{\left(\left(E_j^{pre} - E_i^{pre}\right)^2 + \left(N_j^{pre} - N_i^{pre}\right)^2\right)^2}} \tag{12}$$

Here, $v_{\alpha,ij}$ is the correction to the azimuth observation and θ_{ij} is the computed azimuth. The quantities (N_i^0, E_i^0) and (N_j^0, E_j^0) are the approximate coordinates of nodes P_i and P_j, respectively; $[dN_i, dE_i]$ and $\left[dN_j, dE_j\right]$ are their coordinate corrections. The angular misclosure $l_{\alpha,ij} = wrap(\alpha_{ij}^{obs} - \theta_{ij}^0)$ satisfies $[-\pi, \pi)$. The horizontal distance calculated from the approximate coordinates is $D_{ij}^0 = \sqrt{(N_i^0 - N_j^0)^2 + \left(E_i^0 - E_j^0\right)^2}$, and the corresponding azimuth is $\theta_{ij}^0 = atan2(E_j^0 - E_i^0, N_j^0 - N_i^0)$. The quantities (N_i^{pre}, E_i^{pre}) and (N_j^{pre}, E_j^{pre}) are the preprocessed coordinates of the two nodes, and the corresponding δ terms are their coordinate standard deviations. Under the approximation that correlations among the preprocessed coordinate components are neglected, $\delta_{\alpha_{ij}^{obs}}$ is calculated using the law of error propagation. The coordinate standard deviations in Equation (12) are obtained through simplified uncertainty propagation during preprocessing, with correlation terms neglected. Compass interpolation along the entire streamer, shared head and tail reference positions, and bidirectional coordinate propagation introduce correlations among the preprocessed coordinates. The current implementation neglects these coordinate correlations and treats different derived azimuths as uncorrelated. Thus, the derived azimuths are not new measurements from independent sensors, and the subnetwork posterior covariances are obtained under this engineering approximation.

2.2. Hydrophone Positioning Considering Subnetwork Acoustic Node Constraints

Under steady towing conditions, a submerged streamer generally forms a smooth spatial curve that can be represented by a polynomial function. Assuming that the shape of the k streamer is fitted by a polynomial of degree P, the coordinate vector $\boldsymbol{P}_i = [N_i, E_i]^T$ of a point at design mileage s_i can be expressed as

$$\boldsymbol{P}_i = \boldsymbol{f}(s_i) = \begin{bmatrix} \boldsymbol{S}_i^T \boldsymbol{A} \\ \boldsymbol{S}_i^T \boldsymbol{B} \end{bmatrix} \tag{13}$$

Here, $\boldsymbol{S}_i^T = [1, s_i, s_i^2, \ldots, s_i^p]$ is the streamer mileage vector, and $\boldsymbol{A} = \left[a_0, a_1, \ldots, a_p\right]^T$ and $\boldsymbol{B} = \left[b_0, b_1, \ldots, b_p\right]^T$ contain the unknown polynomial coefficients for the northing and easting components, respectively. A separate set of polynomial parameters is established for each streamer. For n_{str} streamers, the full parameter vector is $\boldsymbol{\beta} = [\boldsymbol{A}_1^T, \boldsymbol{B}_1^T, \ldots, \boldsymbol{A}_{n_{str}}^T, \boldsymbol{B}_{n_{str}}^T]^T$. A sixth-degree polynomial is used to describe the horizontal streamer shape [18]. The same degree is used in the node constraint model and the polynomial comparison model to evaluate the effects of introducing subnetwork node constraints.

The front and rear subnetworks use selected local acoustic ranges and derived line-of-sight azimuths. Acoustic observations used in either subnetwork are excluded from direct use in the global adjustment. Compass observations near the selected nodes that are used for angle interpolation are also excluded from the global observation set. This

allocation prevents the selected direct observations from being used in both stages, although full-streamer compass interpolation and bidirectional coordinate propagation still transmit shared information. The virtual observations retain the posterior covariance matrices of the subnetworks, including correlations among nodes and coordinate components within each subnetwork. The global adjustment uses the virtual coordinate observations derived from the IEKF and the acoustic ranges and compass-azimuth observations retained under the allocation rules described above. The conventional polynomial positioning model directly uses all acoustic distances and compass azimuths; its error equations are described in [20]. For the virtual node observations, once the first-stage IEKF has converged, the coordinates of all unknown nodes in a subnetwork are stacked into a virtual observation vector $\hat{\boldsymbol{P}}_{vir}$. The curve coefficient matrix $\boldsymbol{H}_{vir}$ is constructed in the same node order, giving the following error equation:

$$\boldsymbol{v}_{\hat{\boldsymbol{P}}_{vir}} = \boldsymbol{H}_{vir}\delta\boldsymbol{\beta} - \boldsymbol{l}_{\hat{\boldsymbol{P}}_{vir}} \tag{14}$$

Here, $\boldsymbol{v}_{\hat{\boldsymbol{P}}_{vir}}$ is the correction vector for the virtual observations, $\delta\boldsymbol{\beta}$ is the parameter correction vector, and $\boldsymbol{l}_{\hat{\boldsymbol{P}}_{vir}} = \hat{\boldsymbol{P}}_{vir} - \boldsymbol{H}_{vir}\boldsymbol{\beta}^0$ is the misclosure vector, with $\boldsymbol{\beta}^0$ denoting the approximate parameter values. The virtual coordinate covariance matrices are extracted from the posterior covariance matrices of the front and rear IEKF solutions in the corresponding state order, yielding $\boldsymbol{\Sigma}_{front}$ and $\boldsymbol{\Sigma}_{rear}$. These are assembled as $\boldsymbol{\Sigma}_{vir} = blkdiag(\boldsymbol{\Sigma}_{front}, \boldsymbol{\Sigma}_{rear})$. Combining the error equations for all observations gives the global network adjustment in matrix form:

$$\boldsymbol{V} = \boldsymbol{H}\delta\boldsymbol{\beta} - \boldsymbol{l} \tag{15}$$

Here, $\boldsymbol{V} = \left[\boldsymbol{V}_{rem}^T, \boldsymbol{V}_{vir}^T\right]^T$ is the correction vector for all observations; $\boldsymbol{H} = \left[\boldsymbol{H}_{rem}^T, \boldsymbol{H}_{vir}^T\right]^T$ is the design matrix relating the observations to the polynomial coefficients; $\delta\boldsymbol{\beta} = \left[\delta\boldsymbol{A}_1^T, \delta\boldsymbol{B}_1^T, \ldots, \delta\boldsymbol{A}_{n_{str}}^T, \delta\boldsymbol{B}_{n_{str}}^T\right]^T$ contains the parameter corrections for all streamers; and $\boldsymbol{l} = \left[\boldsymbol{l}_{rem}^T, \boldsymbol{l}_{vir}^T\right]^T$ is the combined misclosure vector.

The front and rear IEKFs are computed separately, but their outputs may be correlated through the propagation of preprocessed coordinates. As an engineering approximation, the cross-covariances between the two subnetwork estimates are neglected. The subsequent global block-diagonal weighting also neglects cross-covariances between the virtual nodes and the remaining observations. Retaining correlations within each subnetwork does not establish statistical independence across the two-stage procedure.

The weight matrix determines how the subnetwork constraints are incorporated into the global adjustment. For the remaining acoustic distance and compass observations, the weight matrix $\boldsymbol{W}_{rem}$ is determined from the nominal sensor precision. For the virtual node observations, the weight matrix $\boldsymbol{W}_{vir}$ is derived from the a posteriori covariance matrix of the IEKF solution. To prevent an excessively small IEKF covariance from imposing overly strong virtual node constraints, a covariance inflation standard deviation σ_ε (a preselected empirical scale, set to 2 m in this study) is introduced:

$$\boldsymbol{W}_{vir} = \left(\boldsymbol{\Sigma}_{vir} + \sigma_\varepsilon^2 I\right)^{-1} \tag{16}$$

The observation weight matrices are then assembled into the global block-diagonal matrix $\boldsymbol{W} = \mathrm{blkdiag}(\boldsymbol{W}_{rem}, \boldsymbol{W}_{vir})$. The polynomial coefficient corrections are obtained by least squares:

$$\delta\hat{\boldsymbol{\beta}} = \left(\boldsymbol{H}^T\boldsymbol{W}\boldsymbol{H}\right)^{-1}\boldsymbol{H}^T\boldsymbol{W}\boldsymbol{l} \tag{17}$$

The initial global parameters are determined from the preprocessed approximate coordinates. The maximum number of iterations is set to 10, and the adjustment at an epoch is considered converged when the prescribed threshold between consecutive iterations is satisfied, $\left\|\delta\hat{\boldsymbol{\beta}}^i - \delta\hat{\boldsymbol{\beta}}^{i+1}\right\|_2 < 0.01$. After convergence, the planar coordinates $(\hat{N}, \hat{E})$ of any

hydrophone are calculated directly by substituting its design mileage s into Equation (13). The formal covariance matrix of the hydrophone coordinates under the adopted weighting model can also be obtained:

$$\boldsymbol{\Sigma}_{(\hat{N},\hat{E})} = \boldsymbol{J}\boldsymbol{Q}_{\hat{\boldsymbol{\beta}}\hat{\boldsymbol{\beta}}}\boldsymbol{J}^{T} \tag{18}$$

Here, $\boldsymbol{J}$ is the Jacobian of the hydrophone coordinates with respect to $\hat{\boldsymbol{\beta}}$, corresponding to the coefficient matrix in Equation (13), and $\boldsymbol{Q}_{\hat{\boldsymbol{\beta}}\hat{\boldsymbol{\beta}}} = (\boldsymbol{H}^{\mathrm{T}}\boldsymbol{W}\boldsymbol{H})^{-1}$ is the parameter cofactor matrix. This propagated matrix describes uncertainty as conditional on the adopted stochastic model and weighting assumptions; it is not an empirically calibrated estimate of hydrophone-position uncertainty.

2.3. Evaluation Metrics for Positioning Deviations

Positioning deviation is defined as the horizontal distance between the estimated and reference coordinates. Acoustic node and hydrophone results are evaluated separately. The simulation uses the generated true coordinates as references, whereas the field experiments use the node coordinates in the P2/94 files [25] and hydrophone coordinates in the P1/90 files [26], produced by a commercial navigation system Field positioning deviations therefore represent differences between the estimated coordinates and the commercial reference solution.

The positioning deviation of an acoustic node is the Euclidean distance between its estimated and reference coordinates at a given epoch. Individual node deviations and their averages within the front and rear subnetworks are calculated at each epoch to describe the temporal distribution of positioning deviations. For acoustic node P_j at epoch i, the deviation between the estimated coordinates $(\hat{N}_j^i, \hat{E}_j^i)$ and reference coordinates $(\widetilde{N}_j^i, \widetilde{E}_j^i)$ is

$$\Delta_j^i = \left[(\hat{N}_j^i - \widetilde{N}_j^i)^2 + (\hat{E}_j^i - \widetilde{E}_j^i)^2 \right]^{\frac{1}{2}} \tag{19}$$

The acoustic nodes are divided into front and rear groups according to the survey configuration. Taking the front group as an example, the mean positioning deviation of its node set $\left\{ P_j \middle| j = 1, 2, \ldots, m_{front} \right\}$ at epoch i is

$$\Delta_{Front}^i = \frac{1}{m_{Front}} \sum_{j=1}^{m_{Front}} \Delta_j^i \tag{20}$$

Here, m_{Front} is the number of unknown front acoustic nodes included in the subnetwork solution. The rear-group mean deviation is calculated in the same manner. Node comparisons use the coordinates of the corresponding nodes from each model's final global positioning solution. Gun-array and tail-buoy nodes used as fixed references are excluded.

Hydrophone positioning deviations are analyzed in both the temporal and spatial dimensions. In the temporal dimension, the arithmetic mean of the deviations of all hydrophones at a given epoch is used to represent the overall positioning deviation at that epoch:

$$d^i = \frac{1}{N_r} \sum_{j=1}^{N_r} [(\hat{N}_j^i - \widetilde{N}_j^i)^2 + (\hat{E}_j^i - \widetilde{E}_j^i)^2]^{\frac{1}{2}} \tag{21}$$

Here, d^i is the mean positioning deviation at epoch i; $(\hat{N}_j^i, \hat{E}_j^i)$ and $(\widetilde{N}_j^i, \widetilde{E}_j^i)$ are the estimated and reference coordinates of hydrophone R_j, respectively; and $N_r = N_{str} \times N_{receiver}$ is the total number of hydrophones, with N_{str} streamers and $N_{receiver}$ hydrophones per streamer. In the spatial dimension, the three models are compared by examining how deviations vary with streamer mileage. The mean deviation at each mileage position over the observation period characterizes the positioning results along different streamer sections. The mean positioning deviation over all epochs is calculated as

$$d_{j,k} = \frac{1}{N_t}\sum_{i=1}^{N_t}[(\hat{N}_{j,k}^{i} - \widetilde{N}_{j,k}^{i})^2 + (\hat{E}_{j,k}^{i} - \widetilde{E}_{j,k}^{i})^2]^{\frac{1}{2}}$$
$$d_j = \frac{1}{N_{str}}\sum_{k=1}^{N_{str}} d_{j,k} \quad (22)$$

Here, $d_{j,k}$ is the temporal mean deviation of the j hydrophone on the k-th streamer, d_j is the corresponding mean across all streamers, and N_t is the total number of observation epochs. The mean, standard deviation, maximum, and minimum are calculated separately for the d^i and d_j sequences to describe temporal and spatial variations. When both statistics use the same complete hydrophone and epoch sets, their overall means are identical.

To assess the uncertainty of the differences in mean deviation between methods, paired difference sequences are constructed from the per-epoch deviation sequences obtained using Equation (21). At each epoch, the proposed model's mean hydrophone deviation is subtracted from that of the comparison model; a positive value indicates a smaller deviation for the proposed method. The stationary bootstrap [27] resamples contiguous epoch segments using identical epoch indices across methods to preserve pairing and within-segment temporal dependence. Mean block lengths of 10, 20, 40, 80, 120, and 160 epochs are tested, and the same block lengths are used for all datasets. Each setting uses 5000 resamples, and the 2.5th and 97.5th percentiles of the bootstrap statistic define the 95% confidence interval. The relative reduction in mean deviation is defined as $\eta = (u_1 - u_2)/u_1 \times 100\%$, where u_1 and u_2 are the sequence means for the comparison method and the proposed method, respectively.

3. Experiments and Results

To assess the mean positioning deviations and temporal variability of the proposed subnetwork-node-constrained method, it is compared with the conventional polynomial model [20] and the hybrid harmonic function model [23] using simulated data and field data acquired by the same survey vessel in two different survey areas. Both comparison models are set to order six, and the proposed method uses a preselected empirical covariance inflation standard deviation of 2 m. All methods use the same input data and the same sets of nodes and hydrophones for evaluation, and all field comparisons are made relative to commercial reference solutions.

3.1. Simulated Data and Positioning Results

The simulated data were generated using SimStr [28], a towed-streamer simulation platform developed by the authors' research team. Based on a streamer dynamics model, the platform simulates underwater streamer motion and outputs P2/94 and P1/90 files in standard positioning data exchange formats for marine seismic surveys. The simulated positioning network comprised six streamers, each 7 km long, with a lateral spacing of 100 m. Each streamer carried 561 hydrophones at 12.5 m intervals and 25 compass birds. Adjacent compass birds were spaced 300 m apart, except for the last pair, which was separated by 100 m. Along-streamer mileage was measured from the first hydrophone on each streamer. The first compass bird was located at 0 m and the first acoustic node at 25 m, while the first and last hydrophones were located at 0 m and 7000 m, respectively. This mileage convention is used in the along-streamer deviation plots below. The acoustic network adopted a front–rear configuration commonly used in survey operations. Two acoustic transducers spaced 75 m apart at the head of each streamer formed the front network with the gun-array transducers. Starting at a streamer mileage of 3500 m, 18 acoustic transducers at 200 m intervals were installed in the middle-to-rear section of each streamer and formed the rear network with the tail-buoy transducers. The survey vessel was equipped with DGNSS

and gyrocompasses, and both the gun arrays and tail buoys were equipped with RGNSS. Figure 4 shows the network configuration. For the IEKF estimation, the front subnetwork comprised the first two rows of streamer acoustic nodes and the gun-array acoustic nodes, while the rear subnetwork comprised the last two rows of streamer acoustic nodes and the tail-buoy acoustic nodes. The gun-array and tail-buoy acoustic nodes served as known reference points, leaving 12 unknown acoustic nodes in each subnetwork. The simulated vessel speed was 2 m/s, with an epoch interval of 10 s and a simulation duration of 10,000 s, yielding 1000 epochs. Zero-mean Gaussian noise with standard deviations of 1.2 m and 1° was added to the acoustic-range and compass-azimuth observations, respectively. All three methods used exactly the same noisy observations.

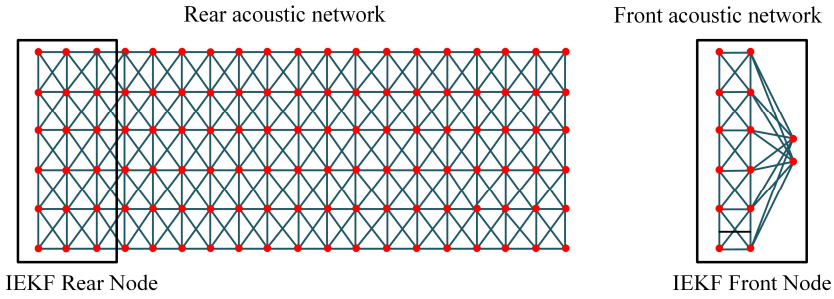

Figure 4. Schematic diagram of the simulated acoustic network configuration.

The effectiveness of the node constraint model is assessed at two levels: the positioning of front and rear acoustic nodes and the final positioning of hydrophones. The acoustic nodes participating in the subnetwork adjustment are examined first, using the true node coordinates recorded in the simulated P2/94 files as references. Figures 5 and 6 show the mean positioning deviations of the front and rear nodes at each epoch, respectively. The node constraint model produces generally smaller deviations and weaker epoch-to-epoch fluctuations than the two comparison methods. As shown in Table 1, the mean front-node deviation decreases from 1.83 m with the polynomial model and 2.41 m with the hybrid harmonic function model to 0.28 m. The corresponding rear-node deviation decreases from 1.25 m and 1.23 m to 0.47 m. The standard deviations of the front and rear deviation sequences are 0.07 m and 0.08 m, respectively, indicating that the subnetwork constraints reduce both the mean node deviations and their temporal fluctuations in this simulation.

The hydrophone coordinates estimated by the three methods are compared with the simulated true coordinates in Figure 7 and Table 2. The proposed method achieves a mean hydrophone positioning deviation of 2.13 m, representing reductions of 19.0% and 24.7% relative to the polynomial and hybrid harmonic function models, respectively. The standard deviation of the per-epoch mean deviation sequence is 0.45 m, compared with 0.53 m and 0.62 m for the two comparison methods. The maximum per-epoch mean deviation decreases from 6.58 m and 6.15 m to 4.83 m. These results show that, under the simulated conditions, the subnetwork constraints reduce both the mean hydrophone deviation and its variation across epochs.

Table 3 presents the paired bootstrap results for the simulated dataset. The proposed method reduces the mean deviation by 0.50 m and 0.70 m relative to the polynomial and hybrid harmonic function models, respectively. At a mean block length of 80 epochs, the corresponding 95% confidence intervals are [0.43, 0.57] m and [0.57, 0.83] m. The intervals remain entirely above zero at all six block lengths, with relatively small changes in their endpoints, consistently supporting a reduction in mean deviation. These results support the observed mean differences in the tested straight-line simulation.

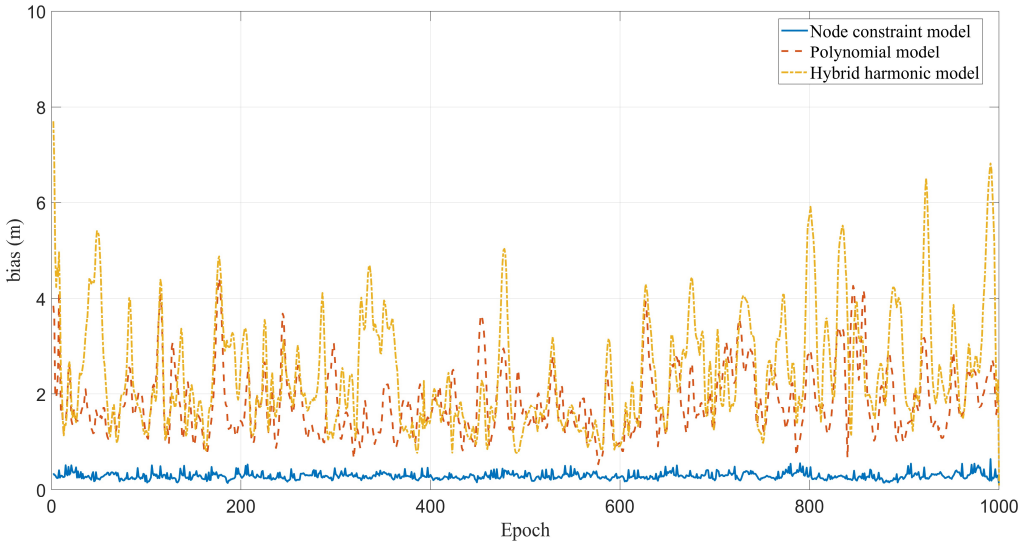

Figure 5. Mean positioning deviation of front acoustic nodes per epoch.

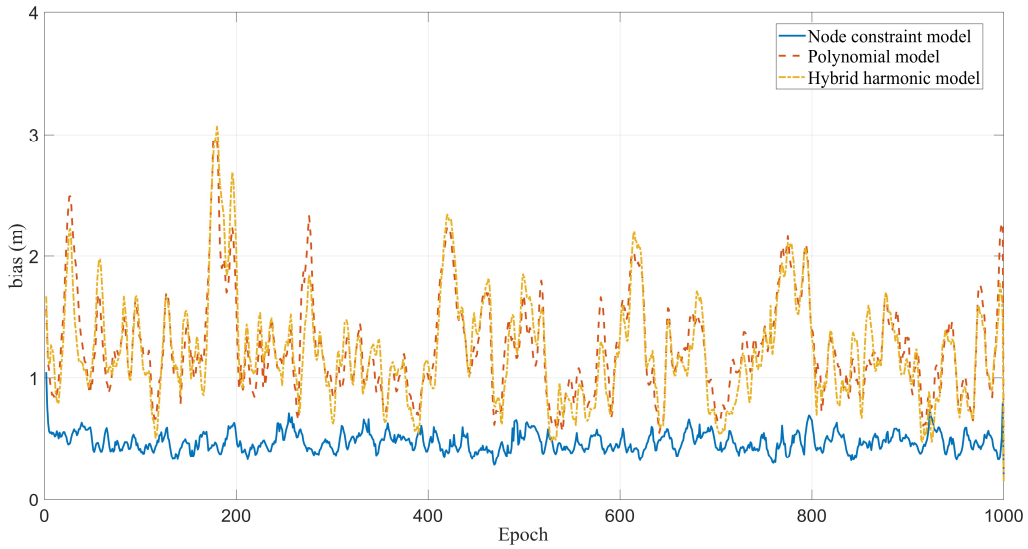

Figure 6. Mean positioning deviation of rear acoustic nodes per epoch.

Table 1. Statistics of mean positioning deviation of subnetwork acoustic nodes per epoch (unit: m).

Model	Subnetwork	Mean	Standard Deviation	Max	Min
Node constraint model	Front network	0.28	0.07	0.63	0.09
	Rear network	0.47	0.08	1.05	0.15
Polynomial model	Front network	1.83	0.70	4.42	0.09
	Rear network	1.25	0.41	2.99	0.15
Hybrid harmonic function model	Front network	2.41	1.16	7.70	0.09
	Rear network	1.23	0.43	3.07	0.15

Figure 8 shows the distribution of mean hydrophone positioning deviation along the streamer, with statistics given in Table 4. All three methods exhibit relatively large deviations in the front-to-middle section. The node constraint model gives smaller deviations at most mileage positions, with a maximum of 5.16 m, compared with 5.45 m and 6.02 m for the polynomial and hybrid harmonic function models. Reductions at the streamer ends and in parts of the middle section indicate that local node constraints affect hydrophone coordinates at different positions through the global curve parameters. The along-streamer standard

deviation of the proposed method is 1.58 m, slightly higher than the polynomial model's 1.51 m but lower than the hybrid harmonic function model's 1.69 m. Thus, the reductions in the mean and maximum deviations do not coincide with a reduction in along-streamer dispersion relative to the polynomial model. As Figure 8 shows, the improvement varies among streamer sections. Relatively large deviations remain in the front-to-middle section, mainly because the lack of acoustic observations in this region allows errors to accumulate during the adjustment.

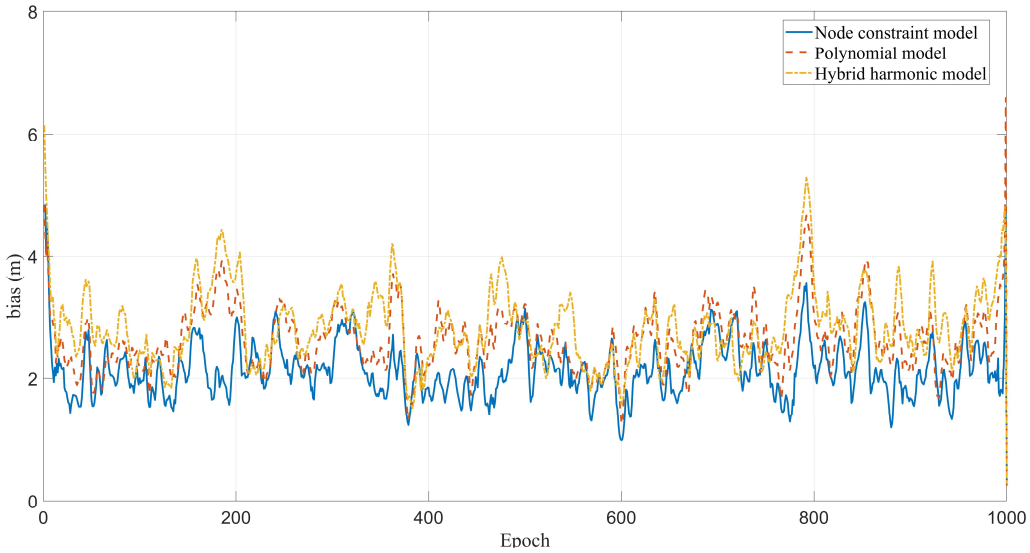

Figure 7. Mean positioning deviation of hydrophones per epoch.

Table 2. Statistics of mean positioning deviation per epoch (unit: m).

Model	Mean	Standard Deviation	Max	Min
Node constraint model	2.13	0.45	4.83	0.24
Polynomial model	2.63	0.53	6.58	0.24
Hybrid harmonic function model	2.83	0.62	6.15	0.24

Table 3. The 95% confidence intervals for mean hydrophone deviation reductions at different mean block lengths (unit: m).

Mean Block Length (Epochs)	Versus Polynomial Model	Versus Hybrid Harmonic Function Model
10	[0.43, 0.58]	[0.58, 0.81]
20	[0.42, 0.58]	[0.57, 0.83]
40	[0.42, 0.58]	[0.56, 0.83]
80	[0.43, 0.57]	[0.57, 0.83]
120	[0.43, 0.57]	[0.56, 0.82]
160	[0.44, 0.56]	[0.57, 0.82]

Table 4. Statistics of mean hydrophone positioning deviation along the streamer (unit: m).

Model	Mean	Standard Deviation	Max	Min
Node constraint model	2.13	1.58	5.16	0.20
Polynomial model	2.63	1.51	5.45	1.18
Hybrid harmonic function model	2.83	1.69	6.02	1.13

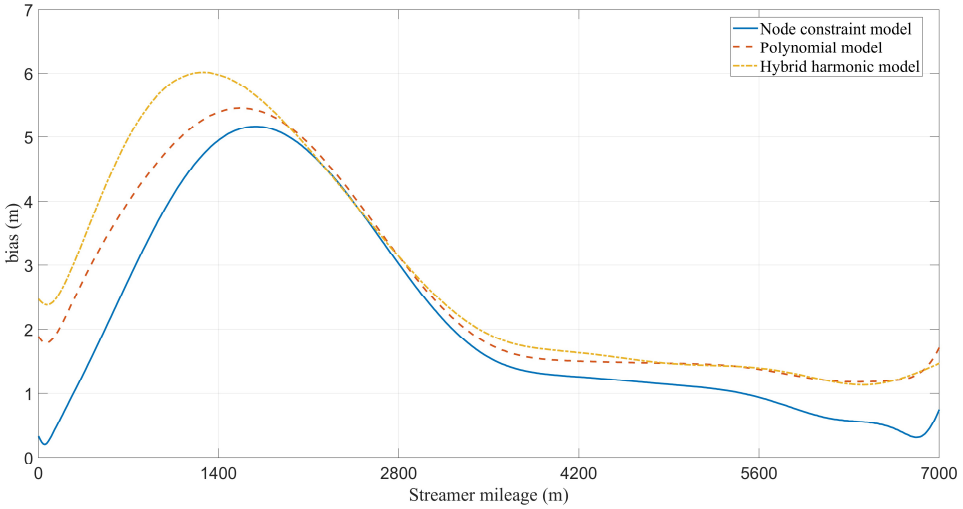

Figure 8. Mean positioning deviation of hydrophones at different streamer mileages.

3.2. Field Data and Positioning Results

Field datasets A and B were acquired by the same survey vessel in two different survey areas. The vessel was equipped with three DGNSS units, three gyrocompasses, and one RGNSS reference station to provide the positioning reference for the network. It towed six streamers, each 6.1 km long, with a lateral spacing of 100 m. Each streamer carried 480 hydrophones at 12.5 m intervals, 23 compass birds, and 17 acoustic transducers. The spacing between the first two compass birds was 30 m, and the successive spacings between the last three compass birds were 250 m and 30 m. All remaining compass-bird intervals were 300 m. The acoustic network adopted a front–rear configuration: three acoustic transducers at the front of each streamer formed the front network with the gun-array transducers, while 14 transducers in the middle-to-rear section formed the rear network with the tail-buoy transducers. Taking the first acoustic node as the start of each streamer, the first compass bird and the first hydrophone were located at along-streamer offsets of 60 m and 100 m, respectively. In the along-streamer deviation plots below, mileage is measured from the first hydrophone; the first and last hydrophones therefore correspond to relative mileages of 0 m and 5987.5 m, respectively. For both field datasets, the acoustic-range and compass-azimuth observations were weighted using their nominal standard deviations of 1.2 m and 1°, respectively.

Datasets A and B contain 684 and 1390 epochs, respectively, both with an observation interval of approximately 10 s. Both datasets were processed using their original observation configurations, without additional artificial observation removal. Figure 9 shows the field network configuration. The front IEKF subnetwork consists of the first three rows of streamer acoustic nodes and the gun-array nodes, while the rear subnetwork comprises the last three rows of streamer acoustic nodes and the tail-buoy nodes. Across the six streamers, each subnetwork contains 18 unknown nodes. Because ground-truth coordinates are unavailable for the field data, the P2/94 and P1/90 files generated by a commercial navigation system [29] are used as references for evaluating acoustic node and hydrophone positioning deviations, respectively.

Dataset A is examined first. Figures 10 and 11 and Table 5 present the positioning results for the front and rear acoustic nodes. For the front nodes, the node constraint model achieves a mean deviation of 1.48 m, lower than the 1.86 m and 1.88 m obtained by the polynomial and hybrid harmonic function models. The maximum decreases from 4.55 m and 4.29 m to 3.46 m. The sequence standard deviation is 0.53 m, slightly higher than the polynomial model's 0.48 m but lower than the hybrid harmonic function model's 0.64 m. Thus, the mean and maximum front-node deviations decrease, but their temporal

dispersion does not decrease relative to the polynomial model. For the rear nodes, the proposed method achieves a mean deviation of 0.89 m, compared with 1.09 m and 1.06 m for the comparison methods. The standard deviation decreases from 0.43 m and 0.44 m to 0.29 m, and the maximum decreases from 2.85 m and 2.71 m to 1.63 m. Unlike the front-node results, the rear-node results improve in mean deviation, temporal variability, and maximum deviation, demonstrating that the subnetwork constraints have different effects in the two node regions.

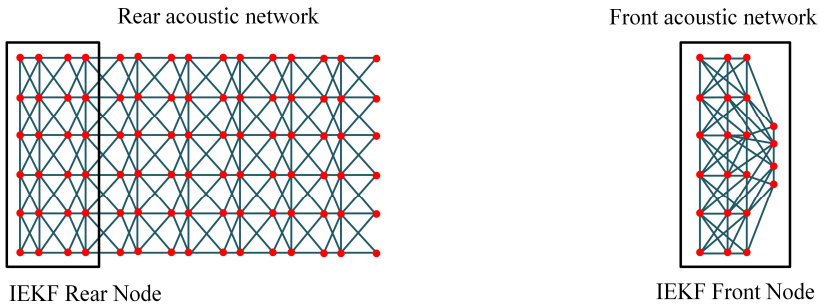

Figure 9. Schematic diagram of the field acoustic network configuration.

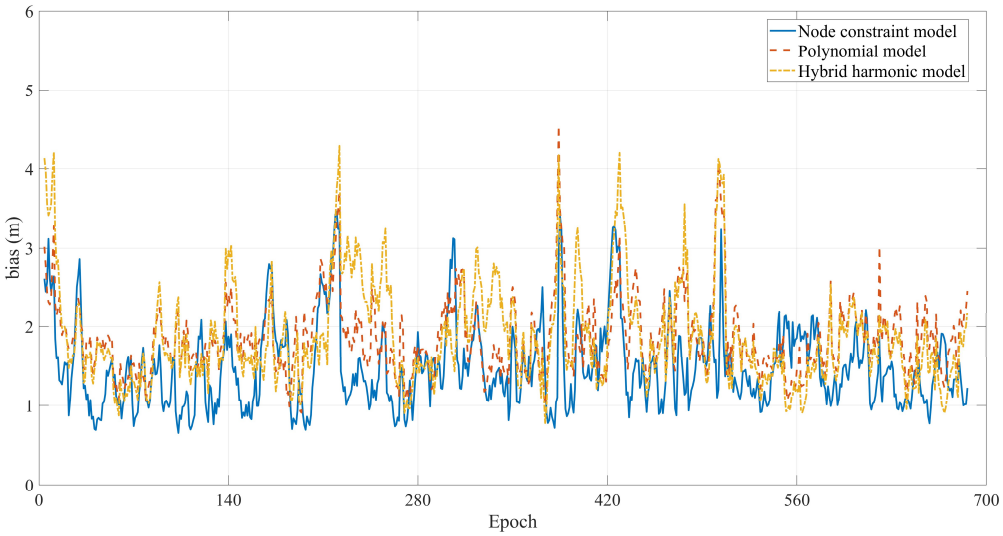

Figure 10. Field dataset A: mean positioning deviation of front acoustic nodes per epoch.

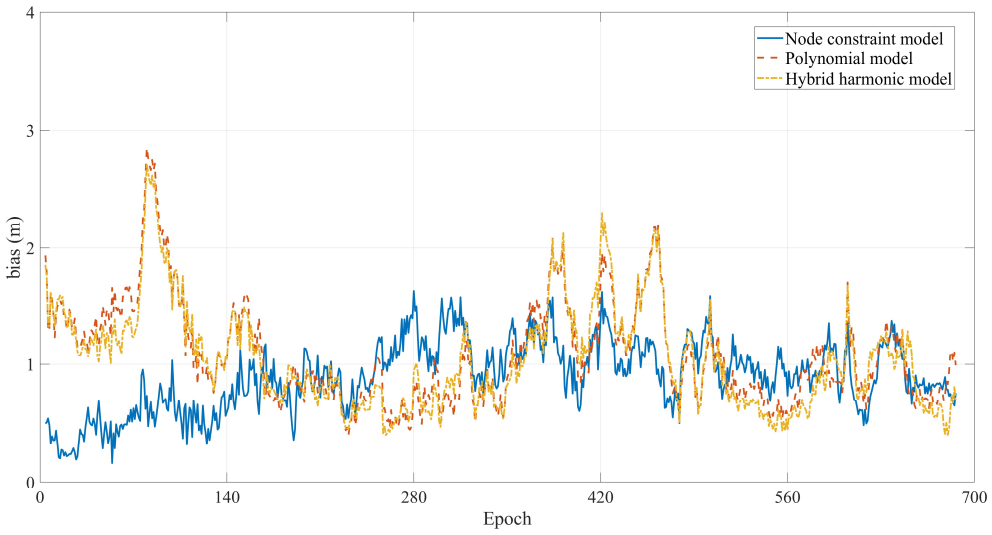

Figure 11. Field dataset A: mean positioning deviation of rear acoustic nodes per epoch.

Table 5. Field dataset A: statistics of mean positioning deviation of subnetwork acoustic nodes per epoch (unit: m).

Model	Subnetwork	Mean	Standard Deviation	Max	Min
Node constraint model	Front network	1.48	0.53	3.46	0.66
	Rear network	0.89	0.29	1.63	0.16
Polynomial model	Front network	1.86	0.48	4.55	0.91
	Rear network	1.09	0.43	2.85	0.40
Hybrid harmonic function model	Front network	1.88	0.64	4.29	0.78
	Rear network	1.06	0.44	2.71	0.40

Figure 12 and Table 6 present the mean hydrophone positioning deviation at each epoch for dataset A. The node constraint model achieves a mean deviation of 3.50 m, representing reductions of 18.8% and 16.5% relative to the polynomial model's 4.31 m and the hybrid harmonic function model's 4.19 m, respectively. Its temporal standard deviation is 0.58 m, compared with 1.06 m and 0.90 m for the comparison methods. The maximum per-epoch mean deviation also decreases from 8.76 m and 7.68 m to 5.84 m. The time series exhibits smaller peaks during several intervals of relatively large deviation and weaker overall fluctuations. These results indicate that introducing subnetwork node constraints reduces both the mean difference between the estimated hydrophone coordinates and the commercial reference solution and its temporal variability.

Table 7 presents the paired bootstrap results for field dataset A. Relative to the polynomial and hybrid harmonic function models, the proposed method reduces the mean discrepancy from the commercial reference solution by 0.81 m and 0.69 m, respectively. At a mean block length of 80 epochs, the 95% confidence intervals are [0.40, 1.28] m and [0.31, 1.13] m, respectively; at 160 epochs, they are [0.36, 1.29] m and [0.28, 1.13] m. All intervals remain entirely above zero across the six block lengths. However, the intervals generally widen as block length increases, with similar results at 120 and 160 epochs. This indicates that uncertainty estimates for the mean differences in dataset A are sensitive to the treatment of temporal dependence, while the reduction in mean discrepancy from the commercial reference remains consistent across the tested block lengths.

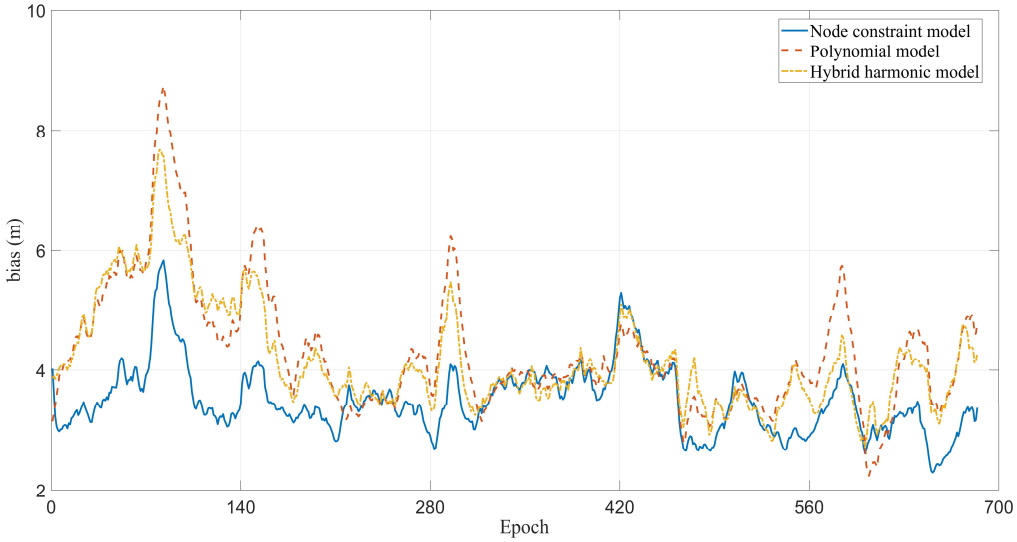

Figure 12. Field dataset A: mean positioning deviation of hydrophones per epoch.

Figure 13 and Table 8 show the along-streamer distribution of mean hydrophone positioning deviation for dataset A. All three methods exhibit relatively large deviations

in the front-to-middle section, followed by an overall decrease toward the tail. The node constraint model gives smaller deviations than the two comparison methods at most middle-to-rear positions, but differs little from the polynomial model near the front-to-middle peak. The maximum along-streamer mean deviation of the proposed method is 6.67 m, slightly higher than the polynomial model's 6.64 m and lower than the hybrid harmonic function model's 7.19 m. Its along-streamer standard deviation is 1.77 m, higher than the corresponding values of 1.44 m and 1.66 m. The reduction in the overall mean therefore mainly results from improvements in certain sections, while the relatively large front-to-middle deviations do not decrease proportionally. Substantial differences among mileage positions consequently remain. This does not contradict the reduction in temporal variability shown in Table 6, because the two statistics describe spatial distribution and temporal variation, respectively.

Table 6. Field dataset A: statistics of mean hydrophone positioning deviation per epoch (unit: m).

Model	Mean	Standard Deviation	Max	Min
Node constraint model	3.50	0.58	5.84	2.29
Polynomial model	4.31	1.06	8.76	2.24
Hybrid harmonic function model	4.19	0.90	7.68	2.71

Table 7. Field dataset A: 95% confidence intervals for mean hydrophone deviation reductions at different mean block lengths (unit: m).

Mean Block Length (Epochs)	Versus Polynomial Model	Versus Hybrid Harmonic Function Model
10	[0.58, 1.06]	[0.49, 0.90]
20	[0.52, 1.14]	[0.43, 0.98]
40	[0.45, 1.22]	[0.35, 1.07]
80	[0.40, 1.28]	[0.31, 1.13]
120	[0.36, 1.30]	[0.28, 1.15]
160	[0.36, 1.29]	[0.28, 1.13]

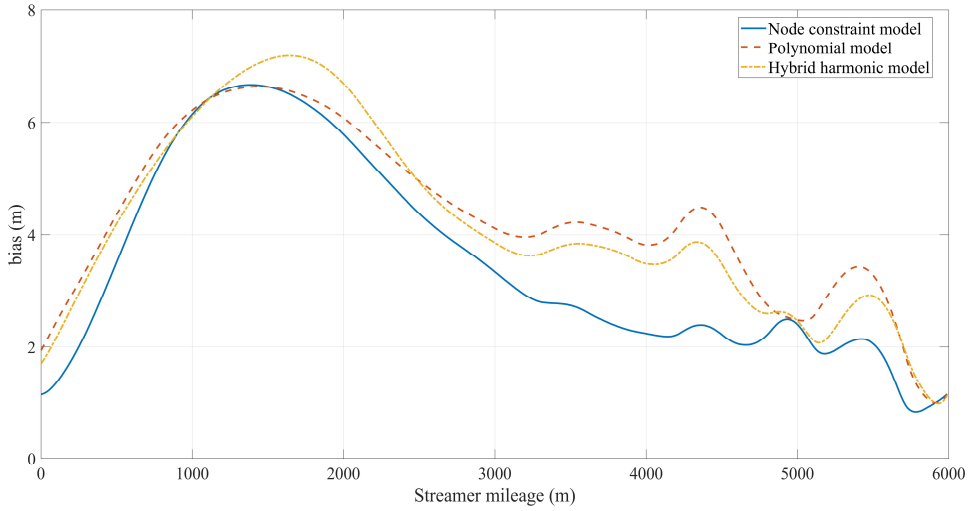

Figure 13. Field dataset A: mean positioning deviation of hydrophones at different streamer mileages.

Dataset B is examined next. Figures 14 and 15 and Table 9 present the positioning results for the front and rear acoustic nodes. For the front nodes, the node constraint model achieves a mean deviation of 2.56 m, compared with 4.22 m and 4.21 m for the polynomial

and hybrid harmonic function models. The sequence standard deviation decreases from 6.58 m and 6.79 m to 1.39 m, and the maximum decreases from 30.37 m and 31.79 m to 10.74 m. In Figure 14, the comparison methods exhibit large deviations at some epochs, whereas the proposed method shows smaller increases over the corresponding intervals. For the rear nodes, the proposed method achieves a mean deviation of 1.51 m, compared with 1.97 m and 1.85 m for the comparison methods. The standard deviation decreases from 0.87 m and 0.84 m to 0.28 m, and the maximum decreases from 6.80 m and 6.71 m to 3.91 m. Compared with dataset A, the node constraints produce more pronounced improvements during intervals with large deviations in dataset B. Both the front and rear nodes exhibit lower mean deviations and weaker temporal fluctuations.

Table 8. Field dataset A: statistics of mean hydrophone positioning deviation along the streamer (unit: m).

Model	Mean	Standard Deviation	Max	Min
Node constraint model	3.50	1.77	6.67	0.84
Polynomial model	4.31	1.44	6.64	1.00
Hybrid harmonic function model	4.19	1.66	7.19	0.99

The hydrophone coordinates estimated by the three methods at each epoch are compared with the reference coordinates in the P1/90 file generated by the commercial navigation system. Figure 16 and Table 10 present the per-epoch mean hydrophone deviations for dataset B. The proposed method achieves a mean deviation of 3.70 m, representing reductions of 22.9% and 18.1% relative to the polynomial model's 4.80 m and the hybrid harmonic function model's 4.52 m, respectively. The temporal standard deviation decreases from 2.30 m and 2.26 m to 0.98 m, while the maximum per-epoch mean deviation decreases from 16.27 m and 16.04 m to 10.43 m. The comparison methods exhibit relatively large deviations over several intervals. The proposed method produces lower peaks in some of these intervals and weaker fluctuations across the sequence. Consistent with the node results, these findings indicate that subnetwork node constraints help reduce large deviations in this dataset. The minimum per-epoch mean deviation of the proposed method is not the lowest of the three methods; its advantage is therefore mainly reflected in the overall mean and in intervals with large deviations, rather than in achieving the smallest deviation at every epoch.

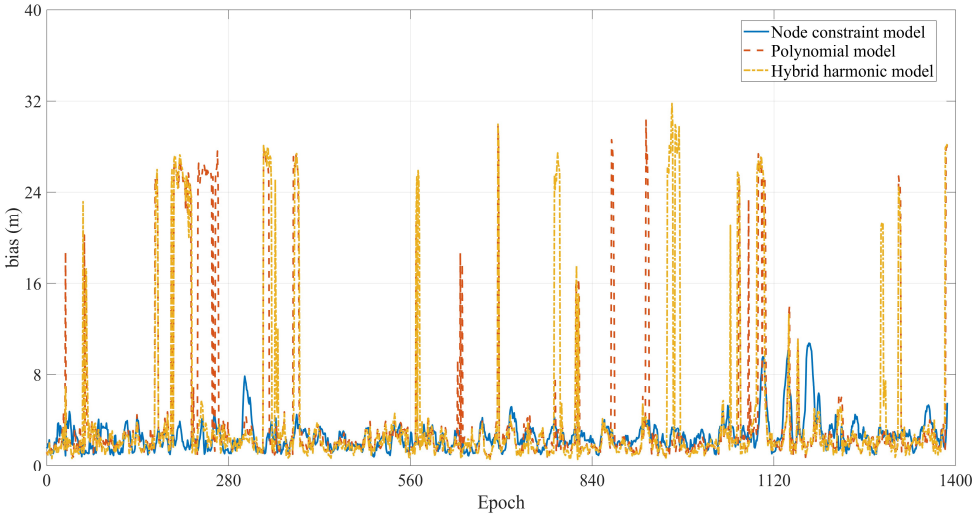

Figure 14. Field dataset B: mean positioning deviation of front acoustic nodes per epoch.

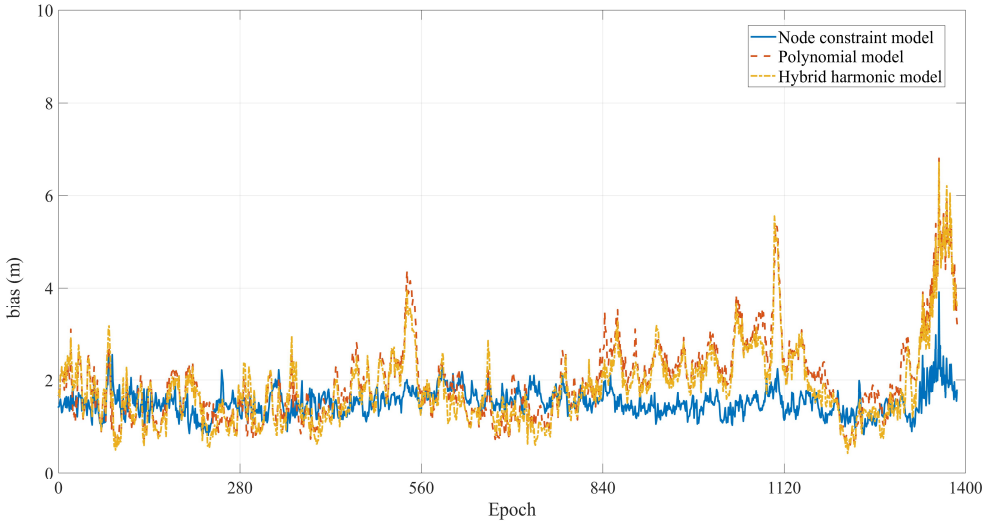

Figure 15. Field dataset B: mean positioning deviation of rear acoustic nodes per epoch.

Table 9. Field dataset B: statistics of mean positioning deviation of subnetwork acoustic nodes per epoch (unit: m).

Model	Subnetwork	Mean	Standard Deviation	Max	Min
Node constraint model	Front network	2.56	1.39	10.74	0.76
	Rear network	1.51	0.28	3.91	0.82
Polynomial model	Front network	4.22	6.58	30.37	0.70
	Rear network	1.97	0.87	6.80	0.52
Hybrid harmonic function model	Front network	4.21	6.79	31.79	0.55
	Rear network	1.85	0.84	6.71	0.42

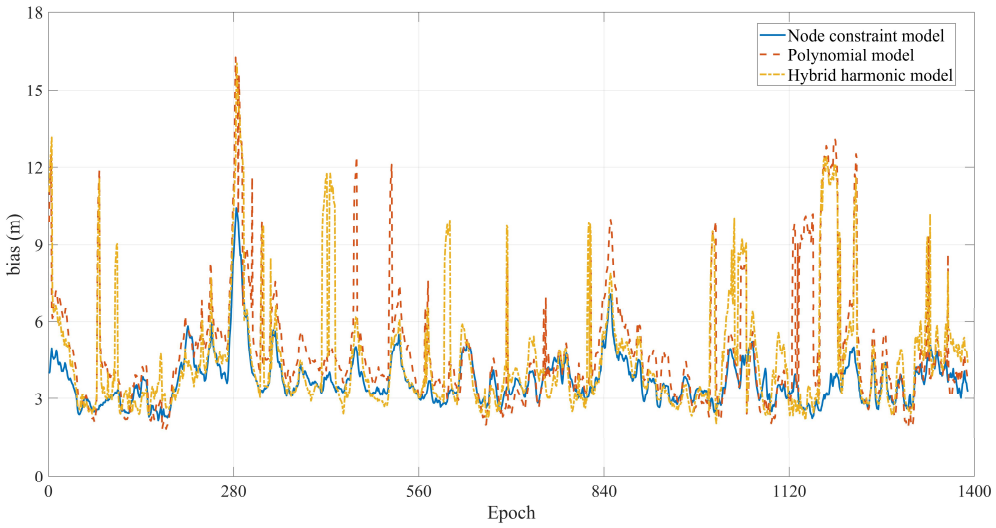

Figure 16. Field dataset B: mean positioning deviation of hydrophones per epoch.

Table 10. Field dataset B: statistics of mean hydrophone positioning deviation per epoch (unit: m).

Model	Mean	Standard Deviation	Max	Min
Node constraint model	3.70	0.98	10.43	2.16
Polynomial model	4.80	2.30	16.27	1.84
Hybrid harmonic function model	4.52	2.26	16.04	2.05

Table 11 presents the paired bootstrap results for field dataset B. Relative to the polynomial and hybrid harmonic function models, the proposed method reduces the mean discrepancy from the commercial reference solution by 1.10 m and 0.82 m, respectively. At a mean block length of 80 epochs, the corresponding 95% confidence intervals are [0.68, 1.64] m and [0.50, 1.21] m. All intervals remain entirely above zero across the six block lengths, supporting lower mean discrepancies from the commercial reference solution for this sequence. The paired statistics quantify mean differences over the complete sequence and do not imply improvement at every epoch.

Table 11. Field dataset B: 95% confidence intervals for mean hydrophone deviation reductions at different mean block lengths (unit: m).

Mean Block Length (Epochs)	Versus Polynomial Model	Versus Hybrid Harmonic Function Model
10	[0.80, 1.45]	[0.55, 1.14]
20	[0.74, 1.54]	[0.51, 1.20]
40	[0.70, 1.60]	[0.50, 1.21]
80	[0.68, 1.64]	[0.50, 1.21]
120	[0.68, 1.59]	[0.51, 1.20]
160	[0.68, 1.58]	[0.52, 1.19]

Figure 17 and Table 12 show the along-streamer distribution of mean hydrophone positioning deviation for dataset B. All three methods exhibit relatively large deviations in the front-to-middle section. The node constraint model gives smaller deviations at most of the plotted positions, with a particularly clear difference from the polynomial model over approximately 3–4.5 km. Its maximum mean deviation is 6.32 m, compared with 6.74 m and 6.95 m for the polynomial and hybrid harmonic function models. The along-streamer standard deviation is 1.34 m, between the corresponding values of 1.21 m and 1.46 m. Relative to the polynomial model, the mean and maximum deviations therefore decrease, but the along-streamer dispersion does not. Together with the results for dataset A, this indicates that the improvement varies among streamer sections. A reduction in the overall mean deviation does not necessarily imply a more uniform distribution of deviations along the streamer.

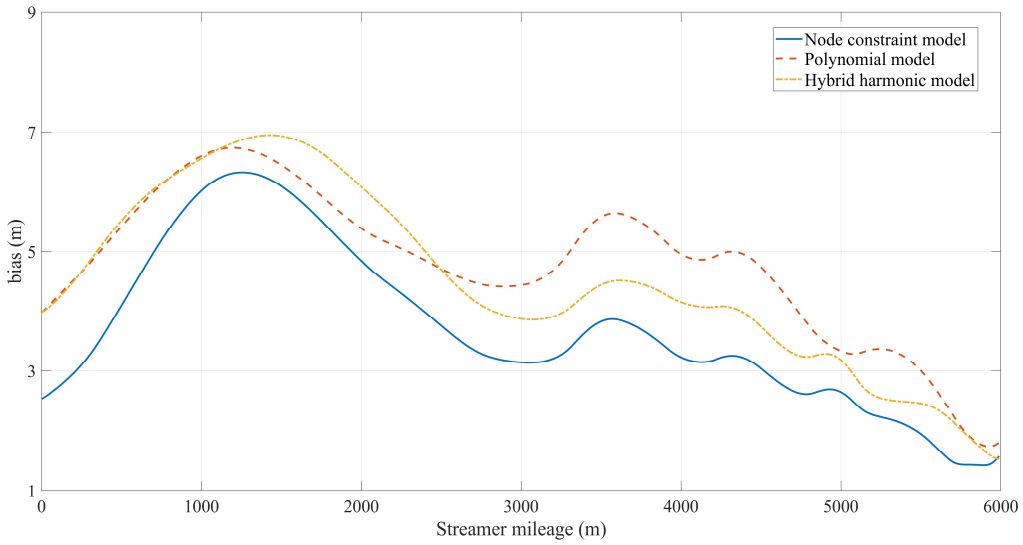

Figure 17. Field dataset B: mean positioning deviation of hydrophones at different streamer mileages.

Table 12. Field dataset B: statistics of mean hydrophone positioning deviation along the streamer (unit: m).

Model	Mean	Standard Deviation	Max	Min
Node constraint model	3.70	1.34	6.32	1.42
Polynomial model	4.80	1.21	6.74	1.73
Hybrid harmonic function model	4.52	1.46	6.95	1.52

3.3. Covariance Inflation Standard Deviation Tests

To examine how the strength of the virtual node constraints affects positioning, the covariance inflation standard deviation σ_ε is set to 0, 1, 2, 3, 4, and 5 m for the simulated and two field datasets. The observation sets, process noise matrices, and all other solution settings remain unchanged within each dataset. Figure 18 shows how the mean hydrophone positioning deviation varies with this parameter, and Table 13 summarizes the results for the front nodes, rear nodes, and hydrophones. The means and standard deviations are calculated from the corresponding per-epoch mean deviation sequences, with the standard deviations representing temporal variability.

As shown in Figure 18 and Table 13, the mean hydrophone deviation in the simulation increases with σ_ε, from 1.88 m at 0 m to 2.95 m at 5 m. The temporal standard deviation also increases, from 0.40 m to 0.63 m. At $\sigma_\varepsilon = 5$ m, the mean hydrophone deviation exceeds those of both comparison methods. Increasing the added variance lowers the virtual node weights and weakens their influence on the global curve, reducing the positioning improvement achieved in this simulation.

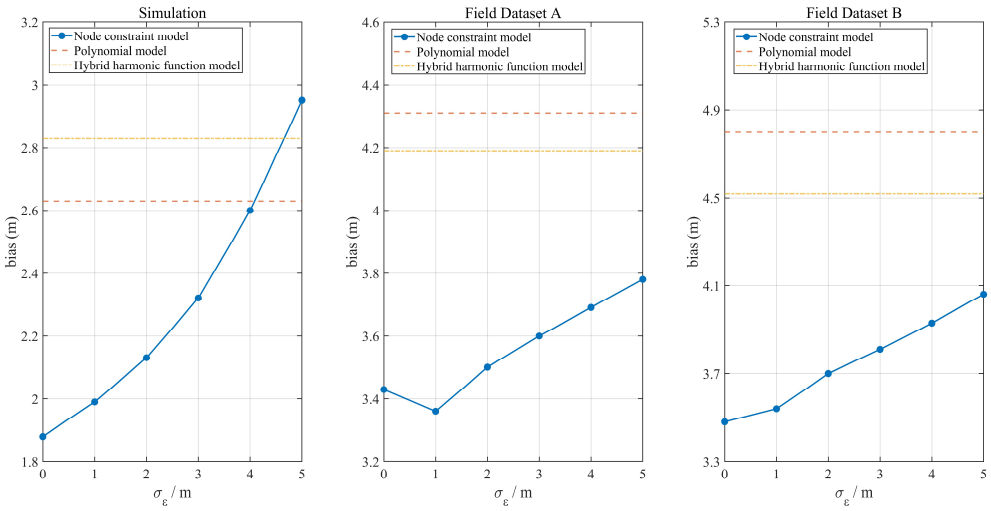

Figure 18. Effect of the covariance inflation parameter on mean hydrophone positioning deviation.

The two field datasets do not follow exactly the same pattern. Dataset A achieves its lowest mean hydrophone deviation, 3.36 m, at $\sigma_\varepsilon = 1$ m, after which the deviation increases with the parameter. Dataset B reaches its minimum of 3.48 m at 0 m and then increases to 4.06 m at 5 m. Across the tested parameter range, the mean hydrophone deviations for both datasets remain lower than those of the two comparison methods, although their temporal standard deviations generally increase with the inflation parameter.

The node and hydrophone deviations also exhibit different trends in the field data. In dataset B, the mean front-node deviation decreases slightly as the inflation parameter increases, whereas the mean hydrophone deviation generally increases. Two factors may contribute to this difference. First, the inflation parameter changes the relative weights of the

virtual nodes and the remaining observations, affecting local nodes and hydrophones along the entire streamer differently. Second, the two metrics use reference coordinates produced at different processing stages. The node references are real-time solutions recorded in P2/94 files, whereas the hydrophone references are postprocessed results recorded in P1/90 files. Differences in processing procedures and error characteristics may therefore produce different responses in the two deviation metrics. Constraint parameters should consequently be selected primarily according to the overall hydrophone positioning results, with node deviations and their temporal variations providing additional information.

Table 13. Positioning deviation statistics for different covariance inflation parameters (unit: m).

Dataset	σ_e	Front Acoustic Nodes		Rear Acoustic Nodes		Hydrophones	
		Mean	SD	Mean	SD	Mean	SD
Simulation	0	0.25	0.07	0.24	0.03	1.88	0.40
	1	0.25	0.07	0.32	0.05	1.99	0.42
	2	0.28	0.07	0.47	0.08	2.13	0.45
	3	0.37	0.09	0.62	0.11	2.32	0.49
	4	0.52	0.14	0.62	0.11	2.60	0.55
	5	0.72	0.20	0.87	0.17	2.95	0.63
Field A	0	1.43	0.48	0.96	0.23	3.43	0.58
	1	1.46	0.48	0.85	0.26	3.36	0.54
	2	1.48	0.53	0.89	0.29	3.50	0.58
	3	1.49	0.55	1.03	0.38	3.60	0.62
	4	1.51	0.56	1.18	0.43	3.69	0.68
	5	1.53	0.58	1.37	0.49	3.78	0.74
Field B	0	2.61	1.38	1.59	0.30	3.48	0.82
	1	2.58	1.39	1.47	0.28	3.54	0.89
	2	2.56	1.39	1.51	0.28	3.70	0.98
	3	2.54	1.39	1.62	0.32	3.81	1.06
	4	2.54	1.41	1.78	0.38	3.93	1.16
	5	2.54	1.40	2.00	0.46	4.06	1.26

3.4. Acoustic Observation Loss Tests

To examine the effects of reduced acoustic observations at the streamer ends, acoustic observations associated with the unknown nodes in the front and rear subnetworks of the simulated dataset are selected as the candidate sets. Observations are randomly removed at rates of 0%, 10%, 20%, 30%, 40%, and 50%. The same removal rate is applied to the front and rear subnetworks. Within each trial, exactly the same observations are removed for all three methods, and each selected acoustic observation is removed throughout the entire epoch sequence to simulate persistent observation loss. The 0% case is run once, while each nonzero loss rate is tested in 10 trials. Removal sets are sampled independently across trials and loss rates. The observation noise and solution settings remain unchanged, and the covariance inflation standard deviation is fixed at 2 m. The reported loss rates refer to the acoustic observations associated with each subnetwork, rather than to all acoustic observations in the global network. Figure 19 and Table 14 summarize the deviations at different loss rates. Each point in Figure 19 represents the mean across trials at the corresponding loss rate, except for the 0% case, which represents a single solution. In Table 14, the value after "±" is the sample standard deviation of the mean deviations from the 10 trials at that loss rate. No between-trial standard deviation is calculated for the single 0% trial.

Figure 19 shows that the mean hydrophone deviations of the polynomial and hybrid harmonic function models generally increase with acoustic observation loss, whereas the node constraint model changes little. As shown in Table 14, at loss rates of 10–50%, the proposed method maintains mean hydrophone deviations of 2.11–2.14 m, with between-trial standard deviations of 0.01–0.02 m. The polynomial model's mean deviation increases from 2.85 m to 3.63 m, while that of the hybrid harmonic function model increases from 2.92 m to 3.82 m. At 50% loss, their between-trial standard deviations reach 0.68 m and 0.55 m, respectively, compared with 0.02 m for the proposed method.

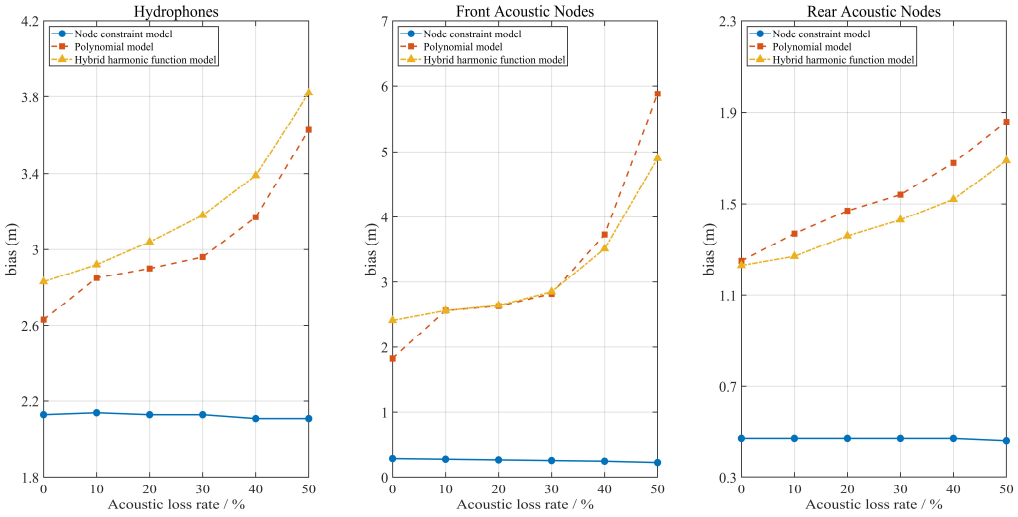

Figure 19. Mean positioning deviation versus acoustic observation loss rate.

The effects of observation loss are more pronounced for the front nodes. At 50% loss, the polynomial and hybrid harmonic function models yield mean front-node deviations of 5.88 m and 4.90 m, with between-trial standard deviations of 3.60 m and 2.23 m, respectively. These results indicate that different removal sets have a considerable influence on their positioning results. The proposed method yields a corresponding mean deviation of 0.22 m and a between-trial standard deviation of 0.01 m. For the rear nodes, its mean deviation remains approximately 0.46–0.47 m, whereas those of the comparison methods generally increase with the loss rate.

For the proposed method, the mean front-node deviation decreases from 0.28 m to 0.22 m as the observation loss rate increases, while the mean hydrophone deviation remains within 2.11–2.14 m. A plausible explanation is the small change in vessel-relative streamer shape between adjacent epochs during the simulated straight-line operation. Under these conditions, the prediction based on the preceding state may already be close to the true state. Removing some acoustic observations may increase the relative influence of the temporal prior and reduce the influence of observation noise on the update, allowing a slight decrease in positioning deviation. This interpretation is consistent with the simulated motion but has not been separately quantified through an ablation analysis. It does not imply that removing observations generally improves positioning accuracy. Across the tested removal sets, the proposed method maintains low mean deviations and small between-trial variations, including at higher loss rates. These results indicate that the combined local temporal estimation and global node constraints can mitigate the effects of persistent end-region acoustic observation loss under the tested straight-line motion and noise conditions.

Table 14. Positioning deviation statistics at different acoustic observation loss rates (unit: m).

Evaluated Object	Loss Rate (%)	Number of Trials	Node Constraint Model	Polynomial Model	Hybrid Harmonic Function Model
Hydrophones	0	1	2.13	2.63	2.83
	10	10	2.14 ± 0.02	2.85 ± 0.05	2.92 ± 0.07
	20	10	2.13 ± 0.02	2.90 ± 0.06	3.04 ± 0.11
	30	10	2.13 ± 0.01	2.96 ± 0.07	3.18 ± 0.11
	40	10	2.11 ± 0.02	3.17 ± 0.41	3.39 ± 0.27
	50	10	2.11 ± 0.02	3.63 ± 0.68	3.82 ± 0.55
Front Acoustic Nodes	0	1	0.28	1.83	2.41
	10	10	0.27 ± 0.01	2.56 ± 0.11	2.56 ± 0.11
	20	10	0.26 ± 0.01	2.63 ± 0.15	2.64 ± 0.14
	30	10	0.25 ± 0.01	2.82 ± 0.22	2.85 ± 0.23
	40	10	0.24 ± 0.01	3.73 ± 2.11	3.51 ± 1.26
	50	10	0.22 ± 0.01	5.88 ± 3.60	4.90 ± 2.23
Rear Acoustic Nodes	0	1	0.47	1.25	1.23
	10	10	0.47 ± 0.01	1.37 ± 0.04	1.27 ± 0.03
	20	10	0.47 ± 0.01	1.47 ± 0.09	1.36 ± 0.07
	30	10	0.47 ± 0.01	1.54 ± 0.10	1.43 ± 0.08
	40	10	0.47 ± 0.01	1.68 ± 0.14	1.52 ± 0.07
	50	10	0.46 ± 0.01	1.86 ± 0.09	1.69 ± 0.08

3.5. Computation Time and Iteration Tests

Introducing subnetwork node constraints adds local IEKF processing before the global polynomial adjustment, so its additional computational cost must be assessed. Under identical software and hardware conditions, the total time required by each method to process all epochs of the simulated dataset and field datasets A and B is recorded, and the average time per epoch is calculated. The computing environment consists of an Intel Core i7-14650HX processor, 16 GB of memory, and CentOS 7.9.2009. The implementation uses GCC 7.3.1, C++17, and Qt 5.12.12, compiled in Release mode with -O2 optimization and executed using a single thread. Wall-clock computation time is recorded using QDateTime::currentDateTime(), excluding P2/94 file reading and P1/90 file output.

As shown in Table 15, the proposed method takes 37.33 s for the simulated dataset, approximately 5.5% longer than the polynomial model's 35.39 s. The additional cost is approximately 1.94 ms per epoch, and the resulting average time remains below the hybrid harmonic function model's 57.01 ms per epoch. For dataset A, the proposed method takes 46.95 s in total, or 68.64 ms per epoch, compared with 72.35 ms and 73.65 ms for the comparison methods. For dataset B, the total is 93.71 s, or 67.41 ms per epoch, again below the comparison methods' 71.90 ms and 89.97 ms. Across the three datasets, the computation time of the proposed method is comparable to that of the polynomial model, and the local IEKF processing does not introduce substantial overall overhead. The two field datasets have similar average times per epoch, while dataset B requires more total time because it contains more epochs. These comparisons show that, for the present implementation and dataset sizes, subnetwork constraints reduce positioning deviations while maintaining computational efficiency comparable to the polynomial model. In addition, the runtime comparison assumes that the dataset-specific process noise matrices have already been estimated offline. It therefore evaluates positioning computation with fixed parameters rather than an end-to-end real-time workflow without future information.

Table 15. Computation times of the three positioning methods.

Dataset	Number of Epochs	Model	Total Time (s)	Mean Time per Epoch (ms)
Simulation	1000	Node constraint model	37.33	37.33
		Polynomial model	35.39	35.39
		Hybrid harmonic function model	57.01	57.01
Field A	684	Node constraint model	46.95	68.64
		Polynomial model	49.49	72.35
		Hybrid harmonic function model	50.38	73.65
Field B	1390	Node constraint model	93.71	67.41
		Polynomial model	99.94	71.90
		Hybrid harmonic function model	125.06	89.97

The node coordinates and covariance matrices produced by the subnetwork IEKF are used directly in the subsequent global adjustment. Iterative convergence is required before the resulting node estimates are used as virtual constraints, and the number of iterations also affects the cost of local processing. To examine local convergence across datasets and observation loss conditions, the mean iteration counts and numbers of nonconvergent solutions are calculated for the front and rear subnetworks of the simulated data at loss rates of 0–50% and for both field datasets. For the nonzero loss rates, the simulation results are averaged across all repeated trials. Table 16 summarizes the results. The mean iteration counts range from 2.00 to 3.10, with no nonconvergent solutions. As the simulated loss rate increases from 0% to 50%, the front and rear mean iteration counts generally decrease from 2.91 and 3.10 to 2.81 and 2.84, respectively. Under the tested conditions, fewer acoustic observations do not increase the local iteration burden, and the subnetwork solutions continue to converge and provide node constraints for the global adjustment.

Table 16. IEKF iteration statistics for the front and rear subnetworks.

Dataset	Loss Rate (%)	Mean Iterations: Front	Mean Iterations: Rear	Nonconvergent Solutions: Front	Nonconvergent Solutions: Rear
Simulation	0	2.91	3.10	0	0
	10	2.91	2.98	0	0
	20	2.89	2.98	0	0
	30	2.86	2.94	0	0
	40	2.87	2.86	0	0
	50	2.81	2.84	0	0
Field A	-	3.07	2.00	0	0
Field B	-	3.03	2.54	0	0

4. Discussion

Introducing subnetwork node constraints reduces the mean hydrophone positioning deviation in all three datasets. The method retains the continuous polynomial representation of the entire streamer and incorporates local filtering results into the global adjustment through node coordinates and their covariance matrices. Its main contribution is the incorporation of information from the end nodes into global parameter estimation while retaining the existing streamer-shape function. Comparisons with the polynomial model of the same degree and the hybrid harmonic function model show lower mean positioning deviations in the tested simulation and smaller mean discrepancies from the commercial reference solutions in the two field datasets. Paired statistics support reductions in mean

deviation across the tested block lengths for these sequences under the fixed implementation and parameter settings; they do not validate the covariance matrices used within the estimator. However, the comparisons evaluate the complete processing chain and do not isolate the individual contributions of the temporal prior, virtual node constraints, covariance weighting, or observation allocation.

The improvement varies spatially, and lower mean deviation does not imply more uniform performance along the streamer. In all three datasets, relatively large mean deviations remain in the front-to-middle region, while some middle-to-rear sections show larger improvements. This pattern may be related to the positioning network configuration. Streamer sections with sparse acoustic observations have weaker direct geometric constraints, so errors in the remaining observations and the fitted curve may have a greater influence on their estimated positions. Because deviations do not decrease proportionally at all positions, the along-streamer standard deviation may increase even when the overall mean decreases. In dataset A, the proposed method has a higher along-streamer standard deviation than both comparison methods but a lower standard deviation of the per-epoch mean deviation. This indicates weaker temporal fluctuations in the overall positioning results, while differences in improvement among streamer positions remain.

Covariance inflation changes the relative weights of the virtual nodes and the remaining observations. Among the tested values, the mean hydrophone deviation is lowest at 0 m for the simulation and field dataset B and at 1 m for field dataset A. The common empirical scale of 2 m is therefore not optimal for every dataset. The current experiments do not establish a general parameter-selection criterion, and increasing the diagonal variances does not reconstruct the neglected cross-covariances. Differences in the responses of node and hydrophone discrepancies to parameter changes may reflect both the spatial effects of the global curve parameters and differences between the reference products. Consequently, a reduction in local node deviation does not necessarily correspond to a simultaneous reduction in hydrophone deviation along the entire streamer.

The field node reference coordinates in this study are taken from real-time solutions recorded in P2/94 files. Their quality is affected by the observations available up to the current epoch, the real-time processing strategy, and observation quality. The hydrophone reference coordinates come from postprocessed P1/90 results, for which the complete observation sequence is available and preprocessing and filtering can be applied. Access to the complete observation sequence allows additional preprocessing and filtering, which may improve consistency but does not establish the absolute accuracy of the reference solution. The two reference solutions may therefore have different error characteristics, affecting how node and hydrophone deviations respond to parameter changes. Because the ultimate objective is hydrophone positioning, parameter assessment should primarily consider the overall hydrophone deviation, with node results used to help interpret the effects of the constraints. Future work could establish node and hydrophone reference solutions under consistent processing conditions.

In the tests with randomly missing end-region acoustic observations, the proposed method shows only small changes in mean deviation across removal sets, and all local IEKF solutions converge. Together with the runtime results, this indicates that adding subnetwork processing does not substantially increase the overall computational burden under the current observation configuration and implementation. The simulated loss tests retain the original noise realization and vary only the sets of end-region acoustic observations removed throughout the complete sequence. Their between-trial standard deviations therefore reflect differences among removal sets. Small changes in streamer shape during straight-line operation favor random-walk prediction, limiting these results to the tested scenario.

The current model retains posterior covariances within each subnetwork but neglects cross-covariances between the front and rear subnetworks, between virtual nodes and the remaining observations, and among derived azimuths. Shared compass interpolation, head and tail references, and preprocessing may introduce these correlations; avoiding direct reuse of observations therefore does not establish statistical independence. Reference coordinates and depths are also treated as known quantities. The effects of these engineering approximations on covariance estimates and final weighting have not been quantified, and the current experiments do not establish strict statistical consistency. The conclusions are restricted to the sixth-degree model, the process noise estimated offline for each dataset, and the tested settings. Further assessment under different noise and motion conditions requires independent reference observations, parameter calibration using independent or withheld data, full correlation propagation, and component ablation studies.

5. Conclusions

We propose a horizontal hydrophone positioning method that incorporates subnetwork node constraints. An IEKF estimates the node coordinates and posterior covariance matrices of the front and rear acoustic subnetworks, and the resulting coordinates are introduced as weighted virtual observations into a global polynomial adjustment. The method retains a continuous functional representation of the entire streamer while incorporating temporal estimates of the local nodes into global streamer-shape estimation. The following conclusions are drawn under the tested straight-line operating conditions and parameter settings.

First, subnetwork node constraints reduce node and hydrophone positioning errors in the simulated dataset and decrease deviations from the commercial reference solution in both field datasets. With a covariance inflation standard deviation of 2 m, the simulated mean deviations of the front and rear nodes are 0.28 m and 0.47 m, respectively. The mean hydrophone deviation is 2.13 m, representing reductions of 19.0% and 24.7% relative to the polynomial and hybrid harmonic function models. For both field datasets, the mean front- and rear-node deviations are lower than those of the comparison methods. The mean hydrophone deviations relative to the commercial reference solution are 3.50 m and 3.70 m, corresponding to reductions of 18.8% and 22.9% relative to the polynomial model and 16.5% and 18.1% relative to the hybrid harmonic function model. Paired stationary bootstrap confidence intervals for the mean reductions remain entirely above zero at all six tested mean block lengths. Temporal fluctuations in the per-epoch mean hydrophone deviations are also reduced in all three datasets.

Second, the proposed method maintains low positioning deviations under the tested conditions of randomly missing acoustic observations at the streamer ends. At loss rates of 10–50%, the mean hydrophone deviation remains within 2.11–2.14 m, with between-trial standard deviations of 0.01–0.02 m—both lower than those of the comparison methods. Subnetwork constraints therefore help reduce the effects of fewer end-region observations and changes in observation combinations on positioning along the entire streamer. The covariance inflation tests also show that constraint strength affects positioning results and should be selected with reference to the overall hydrophone deviation.

Third, the front and rear IEKF solutions converge in all three datasets, with mean iteration counts of 2.00–3.10. The proposed method requires an average of 37.33–68.64 ms per epoch, comparable to the polynomial model. These results indicate that incorporating local node coordinates and their covariances reduces the mean hydrophone deviation in the tested simulation and the mean discrepancy from commercial references in the field datasets, without substantially increasing computational cost.

The present study primarily concerns straight-line seismic acquisition, and its evidence is limited to one simulated noise realization and two field datasets evaluated against commer-

cial reference solutions. Correlations across processing stages and among derived observations are treated approximately, process noise is estimated from complete sequences, and the contributions of individual components and parameter sensitivities have not been separately established. Future work will incorporate independent validation data and independent parameter calibration, refine covariance propagation, and evaluate the method across multiple noise realizations and more complex motion and observation-loss conditions.

Author Contributions: Conceptualization, H.Z. and L.L.; methodology, H.Z. and C.K.; software, H.Z.; validation, H.Z., H.L. and G.G.; formal analysis, H.Z. and B.Y.; investigation, H.Z.; resources, H.Z. and L.L.; data curation, H.Z.; writing—original draft preparation, H.Z.; writing—review and editing, H.Z., L.L., C.K., B.Y., H.L. and G.G.; visualization, H.Z., L.L. and B.Y.; supervision, C.K., L.L. and B.Y.; project administration, C.K. and B.Y.; funding acquisition, C.K. All authors have read and agreed to the published version of the manuscript.

Funding: This research was funded by the Oil & Gas Major Project (No. 2026ZD1403100) and the National Natural Science Foundation of China (No. 42574066).

Institutional Review Board Statement: Not applicable.

Informed Consent Statement: Not applicable.

Data Availability Statement: The datasets presented in this article are not readily available because the data are part of an on-going study. Requests to access the datasets should be directed to the corresponding author (Cuilin Kuang).

Conflicts of Interest: Authors Haonan Zhang and Baocai Yang were employed by the company Geophysical Division of China Oilfield Services Ltd. The remaining authors declare that the research was conducted in the absence of any commercial or financial relationships that could be construed as a potential conflict of interest.

Appendix A

Table A1 lists the process noise standard deviations for the northing and easting components of each estimated node in the three datasets. These values are calculated from demeaned coordinate increments between adjacent epochs in the local coordinate system, and their squares form the diagonal entries of the process noise covariance matrix. The values in each standard deviation column follow the same order as the node names. The smaller values in the simulated dataset reflect the small changes in vessel-relative node coordinates between adjacent epochs during the simulated straight-line operation. In addition, the simulated P2/94 files contain the true node coordinates, so these increments do not include errors from a commercial node-positioning solution. In the field datasets, the coordinate increments may contain both actual changes in streamer shape relative to the vessel and epoch-to-epoch variations in the commercial coordinate errors.

Table A1. Standard deviations of coordinates for the estimated nodes (unit: m).

Dataset	Subnetwork	Node Name	Northing Coordinate Standard Deviation (m)	Easting Coordinate Standard Deviation (m)
Simulation	Front network	S1A1, S1A2, S2A1, S2A2, S3A1, S3A2, S4A1, S4A2, S5A1, S5A2, S6A1, S6A2	0.1535, 0.1178, 0.1534, 0.1226, 0.1535, 0.1262, 0.1534, 0.1262, 0.1534, 0.1226, 0.1534, 0.1177	0.1435, 0.1434, 0.1444, 0.1443, 0.1434, 0.1431, 0.1432, 0.1431, 0.1438, 0.1433, 0.1434, 0.1437
	Rear network	S1A19, S1A20, S2A19, S2A20, S3A19, S3A20, S4A19, S4A20, S5A19, S5A20, S6A19, S6A20	0.1473, 0.1481, 0.1468, 0.1484, 0.1473, 0.1477, 0.1473, 0.1477, 0.1467, 0.1483, 0.1473, 0.1480	0.1436, 0.1444, 0.1426, 0.1439, 0.1450, 0.1450, 0.1442, 0.1446, 0.1428, 0.1426, 0.1428, 0.1424

Table A1. *Cont.*

Dataset	Subnetwork	Node Name	Northing Coordinate Standard Deviation (m)	Easting Coordinate Standard Deviation (m)
Field A	Front network	S1A01, S1A02, S1A03, S2A01, S2A02, S2A03, S3A01, S3A02, S3A03, S4A01, S4A02, S4A03, S5A01, S5A02, S5A03, S6A01, S6A02, S6A03	3.9004, 3.8731, 3.8908, 2.5907, 2.5097, 2.4474, 3.0795, 3.0261, 2.9246, 5.3348, 5.2521, 5.0728, 7.0249, 6.9015, 6.6485, 9.0511, 8.9583, 8.7220	9.5754, 9.4227, 9.1351, 9.0353, 8.8807, 8.5558, 8.2956, 8.1567, 7.8859, 6.7889, 6.6865, 6.5281, 6.2748, 6.0260, 5.7063, 5.4678, 5.2650, 4.9769
	Rear network	S1A09, S1L07, S1A10, S2A09, S2L07, S2A10, S3A09, S3L07, S3A10, S4A09, S4L07, S4A10, S5A09, S5L07, S5A10, S6A09, S6L07, S6A10	7.3056, 7.3984, 7.5991, 6.3839, 6.4609, 6.5760, 6.0538, 6.1518, 6.3323, 6.7603, 6.8553, 6.9337, 7.6323, 7.7626, 7.9179, 9.1905, 9.2837, 9.4001	13.5654, 13.7129, 13.9096, 12.9834, 13.1261, 13.3442, 12.5645, 12.8125, 13.0753, 12.0977, 12.3366, 12.5603, 11.5203, 11.6803, 12.0773, 11.4370, 11.6721, 12.1698
Field B	Front network	S1A01, S1A02, S1A03, S2A01, S2A02, S2A03, S3A01, S3A02, S3A03, S4A01, S4A02, S4A03, S5A01, S5A02, S5A03, S6A01, S6A02, S6A03	8.7287, 8.7323, 8.7276, 5.7465, 5.7274, 5.6935, 5.3561, 5.2956, 5.1455, 4.5326, 4.4780, 4.3616, 6.1391, 6.1151, 6.0504, 9.1801, 9.1662, 9.1395	10.4013, 10.0937, 9.7149, 10.9498, 10.5845, 10.0876, 11.2380, 10.8601, 10.2928, 11.0984, 10.7390, 10.1665, 11.6349, 11.1306, 10.2568, 11.1694, 10.6570, 9.8398
	Rear network	S1A09, S1L07, S1A10, S2A09, S2L07, S2A10, S3A09, S3L07, S3A10, S4A09, S4L07, S4A10, S5A09, S5L07, S5A10, S6A09, S6L07, S6A10	8.8351, 8.8552, 8.9224, 5.5838, 5.6485, 5.7835, 3.4809, 3.5912, 3.7877, 3.1020, 3.1987, 3.3927, 5.5192, 5.5496, 5.6589, 8.8886, 8.8891, 8.9093	17.0503, 17.3836, 18.0816, 16.8004, 16.9881, 17.6804, 16.7544, 17.1076, 18.1321, 17.5081, 17.9715, 18.8970, 17.2501, 17.8886, 19.2384, 17.3336, 18.1411, 19.8643

References

1. Wen, Z.; Wang, J.; Wang, Z.; He, Z.; Song, C.; Liu, X.; Zhang, N.; Ji, T. Analysis of the world deep-sea oil and gas exploration situation. *Pet. Explor. Dev.* **2023**, *50*, 924–936. [CrossRef]
2. Xie, Y.; Yuan, Q. Practice and prospects of deep-water and deep-formation geophysical exploration. *Geophys. Prospect. Pet.* **2023**, *62*, 183–193.
3. Cai, P.; Liu, C.; Lin, Z.; Ming, J.; Fu, Q.; Dong, S.; Zhang, X.; Liu, S.; Feng, N.; Yang, S.; et al. Development strategy of key basic technologies for marine equipment to enhance the marine strength of China. *Eng. Sci.* **2024**, *26*, 91–103. [CrossRef]
4. Wang, S.; Yang, K.; Tang, J. *New Technology and Application of Marine Seismic Exploration*; Petroleum Industry Press: Beijing, China, 2016; pp. 12–19.
5. Wang, X.; Quan, H.; Liu, J.; Luo, M.; Guo, J. *New Progress in Marine Oil and Gas Seismic Exploration Technology*; Petroleum Industry Press: Beijing, China, 2017; pp. 155–157.
6. Ruan, F.; Han, Y.; Qiu, Y.; Zhang, H.; Jing, Z.; Xie, Y. Research progress and application of towed streamer seismic exploration equipment in CNOOC. *Mar. Geol. Front.* **2025**, *41*, 1–9.
7. Zhang, H.; Ruan, F.; Hu, G.; Cui, S.; Qiao, X.; Yuan, P. Key positioning algorithm of marine 3D towed streamer integrated navigation system. *J. Geod. Geoinf. Sci.* **2019**, *36*, 441–446.
8. Gikas, V.; Cross, P.A.; Ridyard, D. Reliability analysis in dynamic systems: Implications for positioning marine seismic networks. *Geophysics* **1999**, *64*, 1014–1022. [CrossRef]
9. Yao, Y.; Yi, W.; Song, W. Processing methods for navigation data of offshore towed streamer exploration. *Geomat. Inf. Sci. Wuhan Univ.* **2010**, *35*, 698–701.
10. Yi, C. Study on Key Techniques of Navigation & Positioning Data Processing and System Development in Marine Seismic Streamer Operation. Ph.D. Thesis, Wuhan University, Wuhan, China, 2013.
11. Yi, C.; Cao, G.; Fang, S.; Sun, S. Fitting of offshore towed streamer shapes. *Geomat. Inf. Sci. Wuhan Univ.* **2010**, *35*, 702–704.
12. Xu, S. Preprocessing method for navigation data of deep-sea streamer exploration. *J. Geod. Geoinf. Sci.* **2014**, *31*, 363–367.
13. Zhang, Z.; Wang, Z.; Dong, S.; Ma, Z.; Qu, C. Integrated navigation and positioning data processing in offshore multi-sources and multi-streamers seismic survey. *Geophys. Prospect. Pet.* **2013**, *52*, 630–635.
14. Sang, K.; Kuang, C.; Yang, Y.; Duan, C.; Zhang, H.; Yang, B.; Ruan, F. Performance evaluation of hydrophone positioning models in marine streamer seismic exploration. *J. Navig. Position.* **2025**, *13*, 76–86.

15. Gilbert, D.C. Seismic streamer position and shape estimation. In Proceedings of the OCEANS 81, Boston, MA, USA, 16–18 September 1981; pp. 1077–1081.
16. Egeland, G. Array shape estimation. In Proceedings of the OCEANS 82, Washington, DC, USA, 20–22 September 1982; pp. 121–122.
17. Zinn, N.D.; Rapatz, P.J.V. Positioning networks in 3D marine seismic. In Proceedings of the Offshore Technology Conference, Houston, TX, USA, 3–6 May 1993.
18. Gikas, V.N. Least Squares Filtering and Testing for Positioning and Quality Control During 3D Marine Seismic Surveys. Ph.D. Thesis, Newcastle University, Newcastle upon Tyne, UK, 1996.
19. Gikas, V.; Cross, P.; Akuamoa, A. Development and testing of mathematical algorithms for source and streamer positioning during marine seismic exploration. In Proceedings of the 57th EAGE Conference and Exhibition, Glasgow, UK, 29 May–2 June 1995.
20. Yu, W.; Wu, P.; Zhang, H.; Hu, G.; Ruan, F.; Dai, W.; Kuang, C. Offshore towed-streamer seismic positioning based on polynomial curve fitting. *Acta Geod. Cartogr. Sin.* **2022**, *51*, 772–780.
21. Duan, C.; Zhang, H.; Kuang, C.; Yu, W.; Ruan, F.; Dai, W. Multi-streamer positioning algorithm based on curvilinear integral for seismic exploration. *Oil Geophys. Prospect.* **2022**, *57*, 1317–1324.
22. Zhang, H.; Sang, K.; Yang, B.; Duan, C.; Lv, L.; Kuang, C.; Liu, H. A spline curve fitting model for towed streamer positioning in marine seismic exploration. *Sensors* **2025**, *25*, 5114. [CrossRef]
23. Sang, K.; Kuang, C.; Lv, L.; Liu, H.; Zhang, H.; Yang, Y.; Yang, B. A hybrid harmonic curve model for multi-streamer hydrophone positioning in seismic exploration. *Sensors* **2024**, *24*, 8025. [CrossRef]
24. Duan, C. Research on Key Algorithms and Software Development for Post-Processing of Offshore Streamer Positioning. Master's Thesis, Central South University, Changsha, China, 2023.
25. United Kingdom Offshore Operators Association. *P2/94: Specification for the Exchange of Raw Marine Positioning Data*; UKOOA: London, UK, 1994. Available online: https://www.iogp.org/wp-content/uploads/2016/12/P2.pdf (accessed on 19 October 2026).
26. United Kingdom Offshore Operators Association. *P1/90: Specification for the Exchange of Marine Positioning Data*; UKOOA: London, UK, 1990. Available online: https://www.iogp.org/wp-content/uploads/2016/12/P1.pdf (accessed on 19 October 2026).
27. Politis, D.N.; Romano, J.P. The stationary bootstrap. *J. Am. Stat. Assoc.* **1994**, *89*, 1303–1313. [CrossRef]
28. Duan, C.; Zhang, H.; Kuang, C.; Yu, W.; Yang, B. SimStr: A C++ program for offshore seismic towed-streamer positioning data simulation. *Geophysics* **2024**, *89*, F11–F21. [CrossRef]
29. Jin, C.; Wang, L. Basic principles and application of ORCA integrated marine navigation system. *Pet. Instr.* **2013**, *5*, 36–40.

Disclaimer/Publisher's Note: The statements, opinions and data contained in all publications are solely those of the individual author(s) and contributor(s) and not of MDPI and/or the editor(s). MDPI and/or the editor(s) disclaim responsibility for any injury to people or property resulting from any ideas, methods, instructions or products referred to in the content.